

The velocity field of the Scorpius-Centaurus OB association

I. Method and general properties

S. Hutschenreuter¹ , J. Alves¹, L. Posch¹, J. Großschedl², M. Piecka¹, N. Miret-Roig^{3, 4}, S. Ratzenböck⁵, and C. Swiggum¹

¹ University of Vienna, Department of Astrophysics, Türkenschanzstraße 17, 1180 Vienna, Austria e-mail: sebastian.hutschenreuter@univie.ac.at

² Astronomical Institute of the Czech Academy of Sciences, Boční II 1401, 141 31 Prague 4, Czech Republic

³ Departament de Física Quàntica i Astrofísica (FQA), Universitat de Barcelona (UB), Martí i Franquès, 1, 08028 Barcelona, Spain

⁴ Institut de Ciències del Cosmos (ICCUB), Universitat de Barcelona (UB), Martí i Franquès, 1, 08028 Barcelona, Spain

⁵ Center for Astrophysics | Harvard & Smithsonian, 60 Garden St., Cambridge, MA 02138, USA

ABSTRACT

We present a non-parametric reconstruction of the three-dimensional velocity field of the Scorpius-Centaurus OB association (Sco-Cen). Using Gaia DR3 astrometry and radial velocities, we infer the velocity field using information field theory on a $70 \times 70 \times 50$ grid at 3 pc resolution. Our model suggests the existence of a primary stellar velocity field with a secondary field that accounts for an additional young kinematic component in Upper Scorpius and Lupus. We find clear tracers of a feedback-driven expansion of the association, while Galactic rotation appears to play a subordinate role. The results confirm the existence of cluster chains and reveal coherent large-scale expansion with characteristic speeds of $1\text{--}2 \text{ km s}^{-1}$ and local maxima of about 10 km s^{-1} . Power spectra indicate an excess of small-scale structure and slopes shallower than Kolmogorov, consistent with energy injection from stellar feedback. Maps of the divergence reveal net positive values, implying an approximate dispersal timescale of 10–15 Myr. A comparison with molecular gas in Lupus and Ophiuchus shows broadly consistent patterns but systematic velocity offsets of several km s^{-1} , suggesting partial decoupling for optically visible young stars and gas. The framework presented provides a physically motivated description of the Sco-Cen velocity field and a basis for quantifying the dynamical state and feedback history of OB associations in the local Galaxy.

Key words. Stars: kinematics and dynamics, ISM: kinematics and dynamics, Galaxy: open clusters and associations: individual: Scorpius-Centaurus, Galaxy: solar neighborhood, Methods: statistical

1. Introduction

The three-dimensional (3D) velocity structure of the interstellar medium (ISM) is a crucial element in understanding the Milky Way's dynamics. Its importance stems from its tight coupling to both the gravitational (via the Boltzmann equation) and magnetic forces (via the MHD equations, cf. flux freezing). Hence, the velocity field(s) of gas, dust, and plasma encode the history and future development of the ISM. Furthermore, these interactions, along with cooling and heating mechanisms, determine the typical lifetimes of structures in the ISM in the order of 10^7 years (McKee & Ostriker 2007; Chevance et al. 2023) and hence provide a natural limit to the inference of the history of the ISM from its own dynamics. Observationally, determining the 3D velocities of any component of the ISM is notoriously difficult, as tangential velocities are mostly inaccessible to direct measurement (with notable exceptions (Piecka et al. 2025)), whereas radial velocities (RVs) are only available for cooler ISM components via Doppler shifts of spectral lines. Thus, the dynamical state and history of the ISM remain largely inaccessible directly due to theoretical and observational limits, apart from special short-lived scenarios such as supernova remnants (e.g., Truelove & McKee 1999).

Young stars offer a promising solution to this problem for two reasons. Firstly, their 3D motion can be measured reliably with spectroscopic and astrometric methods. Furthermore, their initial movement through space depends largely on the condi-

tions of the interstellar medium (ISM) in which they formed, and they only slowly disperse via gravitational interactions (e.g., Zucker et al. 2023). In the case of very young stellar populations, this may allow for the inference of the present-day cloud motions, as demonstrated, for example, in Großschedl et al. (2021). But even as they age, the relatively slow spatial dispersion allows inference of the past location of molecular clouds up to several hundreds of Myr (Swiggum et al. 2024) with a theoretical lower limit at 100 Myr (Arunima et al. 2025).

To connect the dynamics of stars and the ISM, it is necessary to develop a representation of the stellar kinematics that efficiently encodes its spatial distribution and temporal evolution. Traditionally, such analysis is often performed on the cluster level (e.g., Hunt & Reffert 2023), i.e. stellar positions and motions are used to identify distinct groups in the position-velocity phase diagram and then averaged for these clusters, with the idea that these bulk motions capture the original motion of the clusters at their formation, and hence can be used reliably for traceback calculations and isochronal age determination.

In this work, we will take a different point of view and work on the (vector) field level¹, meaning that we view the stars as ‘particles’ constituting a flow which can be treated in the context of fluid dynamics. This has the advantage that we can relate this field directly to ISM-related quantities such

¹ We note that this refers to the physical field concept, and not to the common term ‘field stars’

as energy and momentum densities, and thereby contextualize our results in the picture of the ISM life-cycle in our ever-evolving Galaxy. Furthermore, the field picture allows for an efficient representation of spatial correlations also on small scales, which might get lost in the cluster representation. The value of velocity fields has already been exemplified in cosmology, where the field serves as an important tracer of forces and structure formation processes (e.g., [Stiskalek et al. 2025](#)). We make use of Information Field Theory (IFT) ([Enßlin 2019](#)), a statistical framework that has yielded results on many ISM-related quantities and is especially suited for large non-parametric inference problems and noisy data, as, for example, demonstrated in [Leike & Enßlin \(2019\)](#); [Leike et al. \(2020\)](#); [Hutschenreuter et al. \(2022\)](#); [Edenhofer et al. \(2023\)](#); [Scheel-Platz et al. \(2023\)](#); [Hutschenreuter et al. \(2024\)](#); [Westerkamp et al. \(2024\)](#); [Söding et al. \(2025\)](#).

Of particular interest for the dynamics of the ISM are large complexes of star-forming regions, which can dominate the ISM structure destruction/formation in their immediate surroundings via feedback from supernovae, stellar radiation, and stellar winds ([de Geus 1992](#); [Krause et al. 2018](#); [Alves et al. 2025](#)). By mapping the stellar velocity field, we aim to establish a connection between young stars and their surrounding interstellar medium and to place tighter constraints on the history and future of a large star-forming region.

In this study, we investigate the velocity field of young stars within the Scorpius–Centaurus OB association (Sco-Cen). This nearby and massive star-forming complex provides an important laboratory for studying the interaction between stellar populations and the interstellar medium (ISM). Sco-Cen is currently in an advanced stage of its evolution. Most of its original molecular gas has been consumed or dispersed, with ongoing star formation limited to a few residual regions ([Alves et al. 2025](#)). Over the past ~ 20 Myr, the region has experienced multiple episodes of star formation and supernova activity, events that likely contributed to the formation and shaping of the Local Bubble ([Fuchs et al. 2006](#); [Breitschwerdt et al. 2016](#); [Zucker et al. 2022](#)). The influence of Sco-Cen extends well beyond its immediate environment, with flows of material reaching as far as the Solar System and beyond ([Frisch 1995](#); [Redfield & Linsky 2008](#); [Piecka et al. 2024](#)).

Given its proximity and richness in young stars, Sco-Cen has been extensively studied ([Kapteyn 1914](#); [Blaauw 1946, 1964](#); [de Geus et al. 1989](#); [de Geus 1992](#); [de Bruijne 1999](#); [Makarov 2007b,a](#); [Pöppel et al. 2010](#); [Pecaut & Mamajek 2016](#); [Krause et al. 2018](#); [Wright & Mamajek 2018](#); [Damiani et al. 2019](#); [Forbes et al. 2021](#); [Luhman 2022](#); [Armstrong et al. 2025](#)). Its stellar population exhibits clear evidence of sequential star formation. The oldest subgroups, particularly in the Upper Centaurus–Lupus (UCL) region, have ages of approximately 20 Myr ([Ratzenböck et al. 2023b](#), hereafter R23b). From UCL, stellar age gradients suggest that star formation propagated outward along several filamentary structures or “cluster chains”. These are extending toward the regions of Corona Australis (CrA) ([Posch et al. 2023](#), hereafter P23), Upper Scorpius (USco), Ophiuchus, Lower Centaurus Crux (LCC) ([Posch et al. 2025](#), hereafter P25), and the TW Hydrae Association (TWA) ([Miret-Roig et al. 2025](#), hereafter MR25); see also [Miret-Roig et al. \(2022\)](#) and [Großschedl et al. \(subm.\)](#), hereafter G25).

The ISM structure of Sco-Cen has also been the subject of extensive investigation, covering the cold and dense phases ([Loren 1989](#); [Harju et al. 1993](#); [Zucker et al. 2021](#); [Edenhofer et al. 2024](#)), diffuse atomic and ionized components

([Nehmé et al. 2008](#); [Krause et al. 2018](#)), and magnetic field morphology ([Robitaille et al. 2018](#)). These studies point to a dynamic and possibly turbulent past, but the sequence of events leading to the present-day configuration remains uncertain.

Together, stellar and ISM studies emphasize the importance of Sco-Cen in understanding star formation and feedback processes in the Galactic environment. By mapping the velocity field of its young stellar population, we aim to constrain the dynamical evolution of the association and its interaction with the surrounding ISM. This analysis provides new insight into the star formation history of Sco-Cen and its broader role in shaping the local ISM structure.

Given the range of topics addressed and the novelty of our approach to stellar population analysis, we present this work in three parts: (1) a description of the methodology and general properties of the reconstructed velocity field (Paper I, this paper); (2) an analysis of energy densities and momentum maps (Paper II); and (3) a study of the internal rotation of stellar clusters (Paper III).

2. Data

2.1. Stellar selection, proper motions & distances

A key requirement for our method is a reliable selection of Sco-Cen members. Since field stars are not expected to share the association’s motion, strong contamination would bias results and compromise post-processing. Membership classification was provided by the machine-learning clustering algorithm Significant Mode Analysis (SigMA, [Ratzenböck et al. 2023a](#), hereafter R23a), which detects stellar populations as significant over-densities in 5D phase space $(x, y, z, v_\alpha, v_\delta)$. It applies hierarchical, density-based clustering with a modality test to decide whether density peaks should be merged or retained.

SigMA uses a non-parametric density estimator without explicitly treating heteroscedastic errors. Instead, low-S/N astrometry is removed before clustering, including a strict parallax S/N cut ($\varpi/\sigma_\varpi > 4.5$). Systematically unreliable parallaxes are filtered with the `fidelity_v2` parameter from [Rybicki et al. \(2022\)](#), reducing the sample from ~ 5.5 million to $\sim 980\,000$ *Gaia* DR3 sources in the Sco-Cen volume. From this cleaned set, SigMA identifies 13 103 candidates.

SigMA does not work on the full phase space since it excludes RVs in its analysis and depends on user-defined parameters (e.g., smoothing scale, significance threshold), making some degree of contamination from field stars likely. R23a estimate 5–8%, supported by color–magnitude analysis, but this level is low enough to robustly recover Sco-Cen’s structure and kinematics.

For this sample, we adopt *Gaia* DR3 proper motions and parallaxes ([Gaia Collaboration et al. 2023](#)). No further cuts were applied, as strict criteria are already part of SigMA. Distances are obtained by inverting parallaxes, with distance uncertainties accounted for in our modeling (see Sect.3.3 and AppendixE). We have not used alternative distance estimators (e.g. [Queiroz et al. 2018](#)), as this would lead to inconsistencies with the SigMA results, which were derived from *Gaia* parallaxes.

2.2. Radial velocities

We complement the *Gaia*-based sample with RVs from the compilation of G25, which merges 22 surveys and literature catalogs (see. Appendix A). In contrast to G25, we use an earlier version of SDSS ([Majewski et al. \(2017\)](#), DR17 instead of DR19) and we have additionally added the RV’s of [Frasca et al. \(2017\)](#)

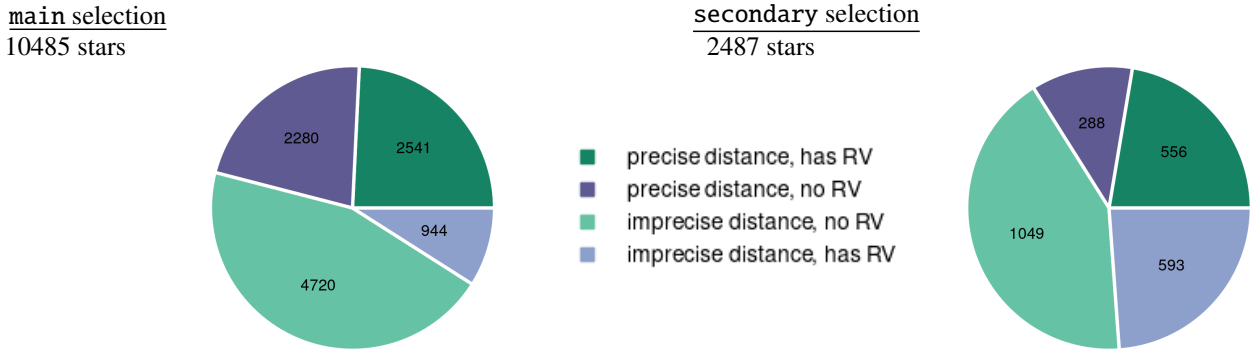


Fig. 1: Illustration of the different categories within our stellar selection.

in the same manner as outlined in G25. The used line-of-sight velocities (spectroscopic RVs) have generally larger uncertainties than the proper motions and may suffer from systematics between surveys or from binarity, which can affect RVs more strongly than astrometry. Appendix A compares the S/N of tangential and radial velocity tracers, highlighting the consistently higher quality of *Gaia* proper motions.

We filtered RVs using the *Gaia* re-normalized unit weight error (RUWE; Castro-Ginard et al. 2024), an indicator of binarity and other systematics. Even after this cut, some RVs may remain affected, which is addressed in our statistical model. The final sample contains 4090 stars with acceptable RVs. Proper motions were not RUWE-filtered, as binarity affects them to a lesser extent.

Based on RV availability and distance reliability, we classify the data into four subsets, summarized in Fig. 1, each requiring specific treatment in the modeling.

3. Method

3.1. Coordinate system and reference frames

In the following, all model components and priors are defined in the heliocentric Cartesian velocity frame, the reference frame of the *Gaia* velocity data. Changing the frame in the model offers no statistical benefit but adds computational cost, while transforming the data into a Sco-Cen frame would alter the error statistics non-trivially.

For our analysis, however, a Sco-Cen-centered frame is required, since quantities like energy and momentum densities are only meaningful there. We therefore converted all posterior field samples in post-processing into the Sco-Cen frame of G25, defined in the barycentric frame by $(v_{x,sc}, v_{y,sc}, v_{z,sc}) = (-6.2, -20.0, -5.4) \text{ km s}^{-1}$. This frame reflects the mean velocity of the oldest Sco-Cen clusters, assumed to trace the association's bulk Galactic motion and be least affected by recent feedback.

Unless noted otherwise, all quantities are expressed in heliocentric Galactic Cartesian coordinates x, y, z on a $70 \times 70 \times 50$ grid with voxel size 3^3 pc^3 , anchored at $(x_0, y_0, z_0) = (-5, -190, -65) \text{ pc}$. Fields on this grid are denoted in boldface, in contrast to stellar models with subscript \star . The cube's extent ensures inclusion of all SigMA stars, and the voxel size reflects typical distance errors in our sample (Sect. 2), which set the spatial scale down to which the data can be expected to be informative. Inferring smaller scales would be possible, but these would likely be constrained mostly by the prior.

We define $\mathcal{P}_{\text{voxel}}$ as the probability that a star lies inside the voxel implied by its parallax and errors, detailed in Appendix A.

A position is flagged as ill-determined if $\mathcal{P}_{\text{voxel}} < 0.682$ (the $1-\sigma$ bound). This threshold balances computational cost from modeling parallax errors with improved accuracy. Under this criterion, $\sim 40\%$ of the sources have reliable distances. In the likelihood description below, we explain how we incorporate uncertainties from the remaining ‘bad’ sources.

3.2. The age structure of Sco-Cen

The ideal picture of OB associations as expanding structures (Blaauw 1964; Quintana 2024) may lead to the expectation of a ‘simple’ (i.e., non-overlapping) corresponding stellar flow field. Complications can arise due to the presence of field stars or the relative acceleration of sub-selections leading to, e.g., velocity caustics. We give a more detailed discussion on the physical field assumption in Appendix B.

Figure 2 shows an orientation plot over the clusters in Sco-Cen as found by SigMA (R23a). The plot clearly reveals the inside-out pattern of star formation in Sco-Cen, with the oldest clusters centered in the middle (around the cluster e-Lup) and clusters becoming progressively younger in all directions from there on. As detailed in Sect. 1, in the specific case of Sco-Cen, the literature gives solid evidence for an accelerated outward expansion of the stellar population for a large volume fraction of the association. The only sub-region that a-priori calls for special attention in this regard is the area towards USco, as the mentioned simple expansion pattern fails here (P25; G25). The results of R23b indicate a more complex age pattern with old and young clusters spatially overlapping. This is a potential problem for our modeling, as this may be indicative of dynamical mechanisms that have accelerated groups of stars towards each other, leading to overlapping flows. A distinction of clusters older and younger than 12 Myr leads to a recovery of spatially distinct age patterns in this region (P25). We have hence flagged eight younger clusters in this part of Sco-Cen (as annotated in Fig. 2) as the ‘secondary’ selection containing 2487 stars, while we refer to the rest of the stars as the ‘main’ selection. We note that the analysis of isochronal cluster ages is a general (non-kinematic) recipe for the pre-analysis of stellar associations with field-based methods to mitigate the intricacies of collisionless flows (see discussion in Appendix B).

These clusters were also selected as outliers based on their peculiar motions in G25, with the sole exception of the cluster L134/L138. The fact that selections based on age and peculiar motion in the region of USco give almost the same result further hints at a source of additional momentum that has impacted this younger selection of stars. It should further be noted that the low

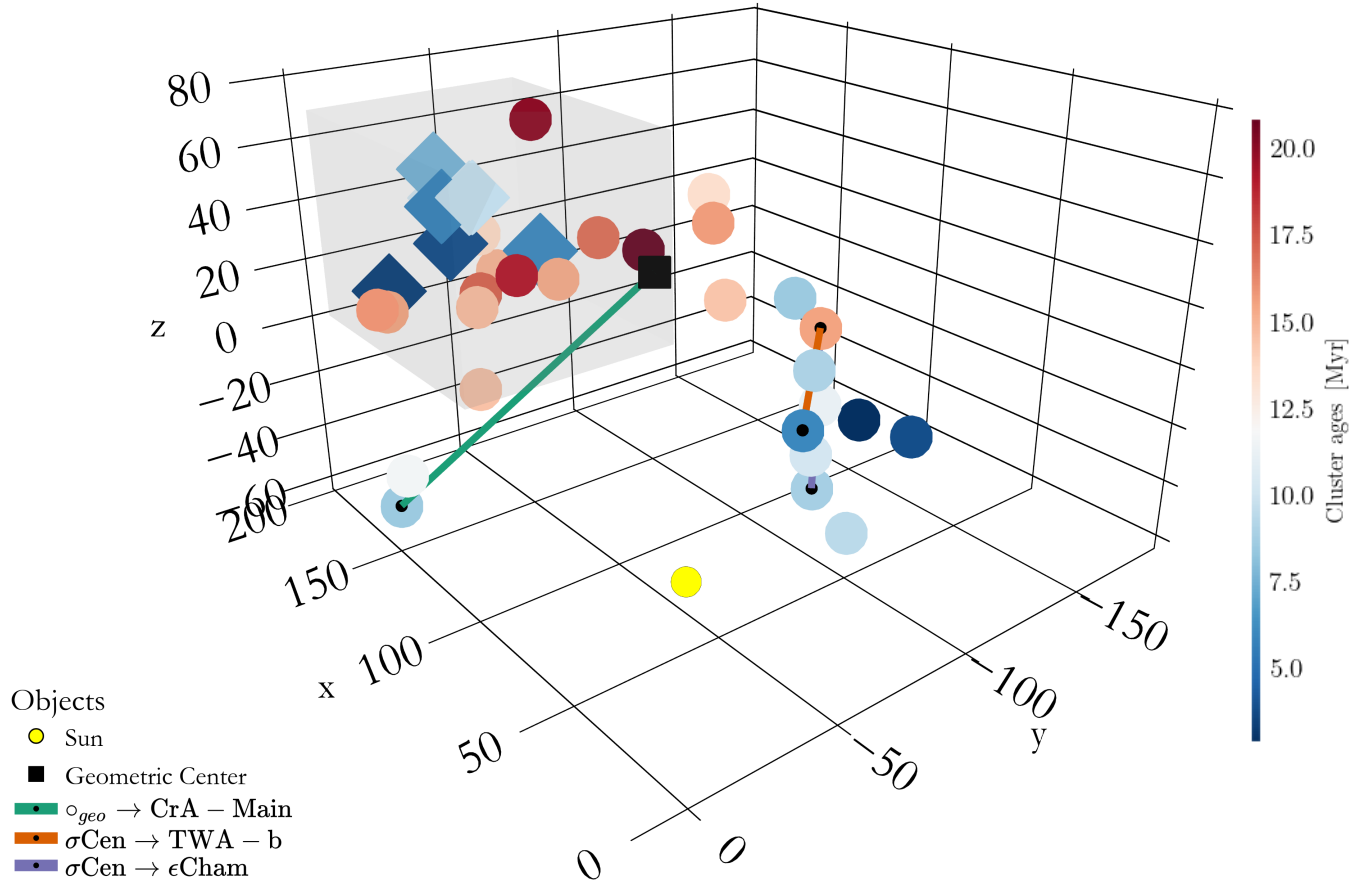


Fig. 2: Orientation plot. This image shows the location and ages of the Sco-Cen clusters (R23a; R23b; MR25). The clusters that contain the stars that we refer to as the **main** sub-selection are shown as spheres, while the **secondary** clusters are shown as diamonds. We shade the volume where the **secondary** selection was performed in gray. The black square indicates the geometric center of Sco-Cen (G25). Additionally, we show three cluster chains as lines. A 3D interactive version of this plot is available [online](#). We note that not all features mentioned are visible in this projection; we refer the reader to the online version for best visibility. Furthermore, individual clusters are identifiable in the online version.

mass cluster L134/L138 is spatially disconnected from USco, and both its age and motion determination rely on a small number of data points, making even this discrepancy of low significance. We would like to emphasize that we have not performed the 12 Myr age cut in the rest of Sco-Cen, as there is no a-priori indication of overlaying velocity structures there. We give details on the clusters within the **secondary** selection in Table A.2.

3.3. Model

3.3.1. Velocity field

The aim is to fit velocity fields $\mathbf{V}_{\text{secondary}}$ and \mathbf{V}_{main} to the proper motions and RVs of stars conditional on their 3D positions $p_{\star} = (x_{\star}, y_{\star}, z_{\star})$. As the motion of the **secondary** selection is likely the result of more recent events (see discussion on ages in Sect. 3.2), we model the velocity field of these stars via a sum of the main velocity field and an additional field \mathbf{V}_{δ} that models the difference between the **main** field \mathbf{V}_{main} and the **secondary** field $\mathbf{V}_{\text{secondary}}$, i.e.:

$$\mathbf{V}_{\text{secondary}} = \mathbf{V}_{\delta} + \mathbf{V}_{\text{main}}. \quad (1)$$

In case there is no second flow present in the true velocity field, the model above would still fit the data, but the \mathbf{V}_{δ} component would get as small as the noise level. For both fields $f \in (\delta, \text{main})$ we write

$$\mathbf{V}_f(x, y, z) = \begin{pmatrix} \mathbf{v}_{x,f} \\ \mathbf{v}_{y,f} \\ \mathbf{v}_{z,f} \end{pmatrix} \quad (2)$$

on a Cartesian grid in Galactic coordinates and in the barycentric velocity frame (see discussion in Sect. 3.1). The components $\mathbf{v}_{x,f}$, $\mathbf{v}_{y,f}$, and $\mathbf{v}_{z,f}$ are each modeled as independent Gaussian random fields with unknown correlation structure. We model this correlation structure via independent power-spectra for all three components for both the \mathbf{V}_{main} and \mathbf{V}_{δ} vector fields. We make use of the field model presented in Arras et al. (2022) and we have for each scalar field component $\mathbf{v}_{i,f}$ with $i \in (x, y, z)$:

$$\mathbf{v}_f = m_{i,f} + \mathcal{F}(\mathbf{A}_{i,f}(k) \xi_{i,f}(k)). \quad (3)$$

Here, $m_{i,f}$ denotes the mean over the full volume, while $\mathbf{A}_{i,f}(k)$ is the amplitude of the scalar component-field in Fourier space (indicated by the wavenumber k), which is directly related to the square root of the power-spectrum. For each component field,

this amplitude field is multiplied with the excitation field $\xi_{i,f}(k)$, which encodes the specific realization of the component, and this product is then Fourier transformed via \mathcal{F} . The power-spectrum itself is modeled via the model presented in [Arras et al. \(2022\)](#), which parametrizes the log-spectrum via the sum of a power-law and a stochastic process. We chose the priors of this model such that the dynamical range both in the means $m_{i,f}$ and the fluctuations around this mean easily encompasses several tens of km s^{-1} . Additionally, we assume a Gaussian prior on the slope of the power-spectrum of the correlation structure of -7 ± 3 . We give further details of the field model prior, as well as choices on hyperparameters, in [Appendix D](#).

3.3.2. From fields to stars

The heliocentric Galactic Cartesian velocity vector of a star belonging to a sub-selection s can be extracted from the respective velocity field via

$$V_{\star,\text{Gal,cart}} = \mathcal{S}_{\star} \mathbf{V}_s, \quad (4)$$

where \mathcal{S}_{\star} is a simple selection operator that returns the value of the field at the position of the star. This is akin to a piece-wise constant interpolation of the voxels. In accordance with our discussion on the effective spatial resolution set by the parallax data (see [Sect. 2](#)), we have refrained from employing more complex interpolation techniques, as these would only have an impact below the 3 pc scale. To be comparable to observations, this vector is converted into the spherical celestial coordinate system (i.e., the International Celestial Reference System, ICRS) via

$$V_{\star,\text{ICRS,sph}} = \begin{pmatrix} v_{\star,\text{RA}} \\ v_{\star,\text{DEC}} \\ v_{\star,\text{R}} \end{pmatrix} = R_{\text{cart} \rightarrow \text{sph}} R_{\text{Gal} \rightarrow \text{ICRS}} V_{\star,\text{Gal-cart}}. \quad (5)$$

The two rotation matrices denote the coordinate transformation from Cartesian to spherical ($R_{\text{cart} \rightarrow \text{sph}}$) coordinates and the rotation between the ICRS and Galactic reference frames ($R_{\text{Gal} \rightarrow \text{ICRS}}$). The proper motion model of the star can then be derived from the two tangential components of $V_{\star,\text{ICRS,sph}}$ via

$$\mu_{\star} = \frac{\varpi_{\star}}{4.74047} \begin{pmatrix} v_{\star,\text{RA}} \\ v_{\star,\text{DEC}} \end{pmatrix}. \quad (6)$$

The RV model of a star RV_{\star} is the third component of $V_{\star,\text{ICRS-sph}}$. With models for the three stellar velocity observables at hand, the last remaining step is the description of the likelihood, incorporating the fact that the position of some stars is not known with sufficient certainty.

3.3.3. Likelihood

We connect the μ_{\star} and RV_{\star} models to the data in the likelihood, where we have to consider the different cases in our data set outlined in [Sect. 2](#) and [Fig. 1](#), namely whether the stars belong to the secondary sub-selection, whether they have RV measurements, and whether they have a precisely determined distance w.r.t. our computational grid (see [Sect. 3.1](#)). The simplest cases arise for the stars where we have precise distance data, and can replace the model for the distance of the star p_{\star} with the observed position p determined from parallaxes, $|p| = 1/\varpi$, and sky positions (RA, DEC). In particular, for the cases where we have only proper motion data and under the assumption of Gaussian noise, the likelihood is

$$\mathcal{P}_{s,1}(\mu | \mathbf{V}_s, \varpi) = \mathcal{G}(\mu - \mu_{\star}(\mathbf{V}_s, p), C_{\mu}). \quad (7)$$

The symbol $\mathcal{G}(x - m_x, C_x)$ denotes a multivariate Gaussian distribution in quantity x , with mean m_x and covariance C_x . In the equation above, C_{μ} specifically is the noise covariance matrix reported by *Gaia*. If an RV is observed for a star, we can exploit the independence of proper motion and RV measurements and write:

$$\begin{aligned} \mathcal{P}_{s,2}(\mu, \text{RV} | \mathbf{V}_s, \eta_{\text{RV}}, \varpi) &= \mathcal{P}(\mathcal{D}_{\mu} | \mathbf{V}_s, \varpi) \mathcal{P}(\mathcal{D}_{\text{RV}} | \mathbf{V}_s, \eta_{\text{RV}}, \varpi) = \\ &= \mathcal{G}(\mu - \mu_{\star}(\mathbf{V}_s, p), C_{\mu}) \mathcal{G}(\text{RV} - \text{RV}_{\star}(\mathbf{V}_s, p), \eta_{\text{RV}} \sigma_{\text{RV}}^2) \end{aligned} \quad (8)$$

For the observational errors of the RVs, we have introduced an additional model parameter η_{RV} per RV measurement to modify the noise term of the RV likelihood:

$$\tilde{\sigma}_{\text{RV}}^2 = \eta_{\text{RV}} \sigma_{\text{RV}}^2. \quad (9)$$

This factor has an inverse-gamma prior chosen such that the most likely value is unity. This implies that we a-priori trust the observational errors, but the heavy tail of the inverse-gamma distribution allows for an effective down-weighting of outliers caused, for instance, by binarity (see discussion in [Sect. 2](#)), if necessary. We discuss hyperparameters of this part of the model in [Appendix D](#) and refer the reader to [Oppermann et al. \(2012\)](#) for the motivation of the inverse-gamma prior.

For the subset of stars with large distance errors compared to the voxel size (see [Sect. 3.1](#)), we need to incorporate the uncertainty stemming from the parallax measurements. We then include the parallax uncertainty by marginalizing over the positions of the stars conditional on the parallax data. The dependence of the velocity field estimate on the uncertainty of the stellar position is generally not analytically tractable, as its impact depends on the structure of the velocity field itself. To tackle this, we follow the prescription of [Leike & Enßlin \(2019\)](#); [Edenhofer et al. \(2023\)](#) to derive an additional noise term in the likelihood; we give a derivation specific to our setup in the [Appendix E](#). This works under the assumption that we can approximate the additional parallax error term via sampling the model at different distances according to the respective parallax error and estimating a (Gaussian) error term from that, leading to the following expressions for the likelihood, again for the cases without measured RV

$$\mathcal{P}_{s,3}(\mu | \mathbf{V}_s, \varpi) \approx \mathcal{G}(\mu - \langle \mu_{\star} \rangle_{\varpi}, C_{\mu} + \langle C_{\mu} \rangle_{\varpi}) \quad (10)$$

and for stars with measured RV

$$\mathcal{P}_{s,4}(\mu, \text{RV} | \mathbf{V}_s, \varpi) \approx \mathcal{G}\left(\left(\frac{\mu}{\text{RV}}\right) - \left(\frac{\langle \mu_{\star} \rangle_{\varpi}}{\langle \text{RV}_{\star} \rangle_{\varpi}}\right), C_{\mu,\text{RV}} + \langle C_{\mu,\text{RV}} \rangle_{\varpi}\right). \quad (11)$$

The notation $\langle x_{\star} \rangle_{\varpi}$ and $\langle C_{\mu,\text{RV}} \rangle_{\varpi}$ indicates mean and covariance estimated from the model realization for a quantity x evaluated at different stellar distances; we give their definition in [Appendix E](#). The error estimate from the parallax uncertainties couples the RV and proper motion likelihoods, hence making $\langle C_{\mu,\text{RV}} \rangle_{\varpi}$ a full 3×3 matrix per star. We note that the asymmetry of the distance distribution induced by inverting the parallax sample is fully accounted for in our model. The only strong assumption is the Gaussianity of the additional error term, which is a first order approximation. The statistics of this term depend on the distance sampling relative to the typical scales of the velocity field, which is a-priori unknown.

Gaia does not only report cross-correlations between the proper motion components of the stars, but also between proper motion and parallax. The latter term can be ignored in our setup,

as we are not fitting the parallaxes but marginalizing over them, which implicitly incorporates any model cross-correlation between these quantities, while the data cross-correlation is not informative due to the marginalization.

Given all the above considerations, the full likelihood is then the product of all eight sub-selection likelihoods:

$$\mathcal{P}_{\text{full}}(\mu, \text{RV} | \mathbf{V}, \varpi) = \prod_s \prod_{i=1}^4 \mathcal{P}_{s,i}(\mu, \text{RV} | \mathbf{V}_s, \varpi) \quad (12)$$

The subscript s runs over the main and secondary selection of stars. We give the details of the derivation in Appendix E.

3.4. Inference

The model described above has 5 027 299 degrees of freedom, entailing 4 800 006 field parameters, 222 600 power spectrum parameters, and 4 634 noise estimation parameters. We note that the number of field and power spectrum parameters mostly depend on the spatial and spectral resolution chosen in our model. The number of noise estimation parameters is the number of stars with reliable RV measurement; see discussion in Sect. 2.

A full evaluation of such a high-dimensional and non-Gaussian posterior probability distribution is computationally extremely challenging. We hence employ a variational inference scheme, which means we infer a simpler and more tractable distribution to approximate the high-dimensional and likely very complex structure of the posterior. Specifically, we employ geometric variational inference (GeoVI, Frank et al. 2021), in which the posterior is approximated by a multivariate Gaussian distribution augmented with a coordinate transformation constructed from Riemannian geometry and the Fisher information metric, which captures non-Gaussian aspects of the true posterior. For a detailed discussion of the method and comparison to other ways to evaluate posterior distributions, we refer the reader to Frank et al. (2021).

4. Results

In the following, we present the results of the inference setup laid out in the sections above. We evaluate the resulting approximated posterior via drawing samples from it and report the corresponding empirical mean and standard deviations for the model and some of its components online². Additionally, we publish the latent space samples as well as the computational model online, for full reproducibility of our results. The full statistical uncertainty is only captured in the latent space samples. For example, cross-voxel correlations are lost if only the statistical standard deviation on the field level is considered. We hence recommend the usage of the latent samples if the full statistical information is needed for further analysis.

Results on the velocity fields, the power spectra and the divergence of the main field are shown in the following sections, while results on the noise estimation factors are given in Appendix F, on the component fields in Appendix G, and on some of the derivative fields in Appendix H. All two and 3D plots depict the posterior mean; we have refrained from visualizing the statistical uncertainties in these cases. These can be derived from the latent samples and the model². Interactive versions of the plots are available online³. For one-dimensional plots and numerical values, we show the propagated statistical uncertainties.

4.1. Velocity Field

We show a projection of the main result, the posterior mean of the main and secondary velocity fields, in Fig. 3a in the reference frame defined by G25. Additionally, we show the secondary velocity field associated with the secondary sub-selection in Fig. 3b and the difference of this field to the main field in Fig. 3c. In these plots and all following plots, we define the border of the main and secondary volume via a mass-weighted kernel density estimate using the SigMA selection of stars at $\rho_\star = 0.005 \text{ pc}^{-3}$. For reference, we show a contour plot of the stellar density in Appendix C. Quantitatively, we summarize the minimum and maximum values, their position in the grid, and the root-mean-square (rms) values of the main, secondary, and the δ fields in Table 1.

Visually, the plot in Fig. 3a confirms the expanding velocity pattern of the flow already found in P23; G25. In combination with the age of the clusters found by R23b, this visual pattern alone already paints a convincing picture of Sco-Cen as an aging star-forming complex that experienced "inside-out" star-formation, where the star-forming gas reservoir was constantly accelerated, a process that has left its imprints in the stellar kinematics. The main body of Sco-Cen seems to expand from a flow origin at $(x, y, z) = (106 \pm 38, -70 \pm 27, 27 \pm 15) \text{ pc}$, (G25). This expansion manifests itself as a bulk motion towards the known secondary centers of star formation in USco and σ -Cen (R23b; G25) and via relatively narrow chains of stars accelerated away from the older parts of Sco-Cen (c.f., Fig. 2 and P25; MR25).

The secondary velocity field depicted in Fig. 3b has a higher maximum value than the main field, which, moreover, is placed in the youngest member cluster, the B59 cluster. This is consistent with the ongoing feedback-driven momentum input to star-forming clouds.

The difference between the main and secondary velocity field, V_δ (see Eq. 1), is illustrated in Fig. 3c and is dominated by two distinct features. One is a systematic shift in the negative v_z direction and a positive direction in the bulk of USco, which was already noted in G25; P25. The second notable feature is the location maximum of the flow (see Table 1), which is centered right within the Lupus 1–4 cluster, and almost fully explains the respective field values in the secondary field. This means that this relatively young stellar cluster has a motion completely distinct from the rest of the bulk motion of Sco-Cen, which, given the age, must indicate a strong momentum impact to the progenitor cloud of Lupus 1–4 or it being an unrelated structure within the Sco-Cen volume. We note that USco and specifically the interface between the Lupus and Ophiuchus molecular clouds have been under the influence of recent supernovae events (Breitschwerdt et al. 2016; Neuhäuser et al. 2020; Briceño-Morales & Chanamé 2023) and ongoing radiative feedback (Alves et al. 2025). A connection of the morphology and energy density of the flow to these recent events will be pursued in Paper II.

4.2. Power spectra and divergence

We furthermore calculate several secondary quantities, namely power spectra and derivatives. We depict the posterior samples and means of the power spectra of each component of the main and δ flows in Fig. 4, and report the posterior values of the slope parameters in Table 1.

In case of the main flow power spectra shown in Fig. 4a, we report that the slopes are consistently higher than the Kolmogorov value of $-11/3$, implying that small scales have sig-

² <https://zenodo.org/records/17107581>

³ https://shutsch.github.io/sco_cen_data.html

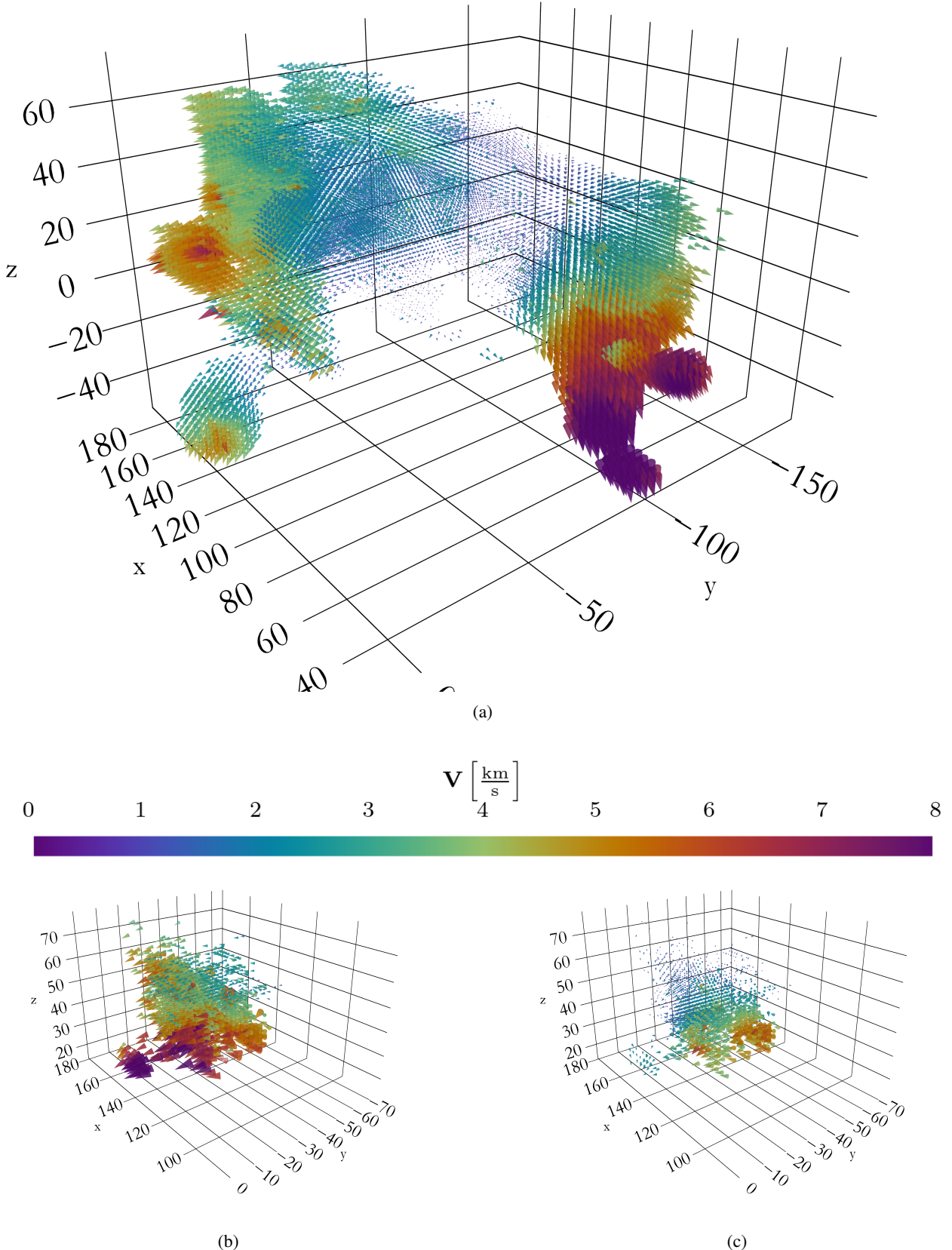


Fig. 3: Posterior mean of the flow fields in the velocity reference frame of G25. For each plot, we have defined a mask using the density of stars to highlight only parts of the volume that were directly informed by data as described in Sect. 4.1. Fig. 3a depicts the main field, while Figs. 3b and 3c depict the secondary and δ field. These projections of the vector fields can naturally only provide a first impression and might locally be misleading; for a better depiction, we refer to the 3D interactive version of these plots available [online](#).

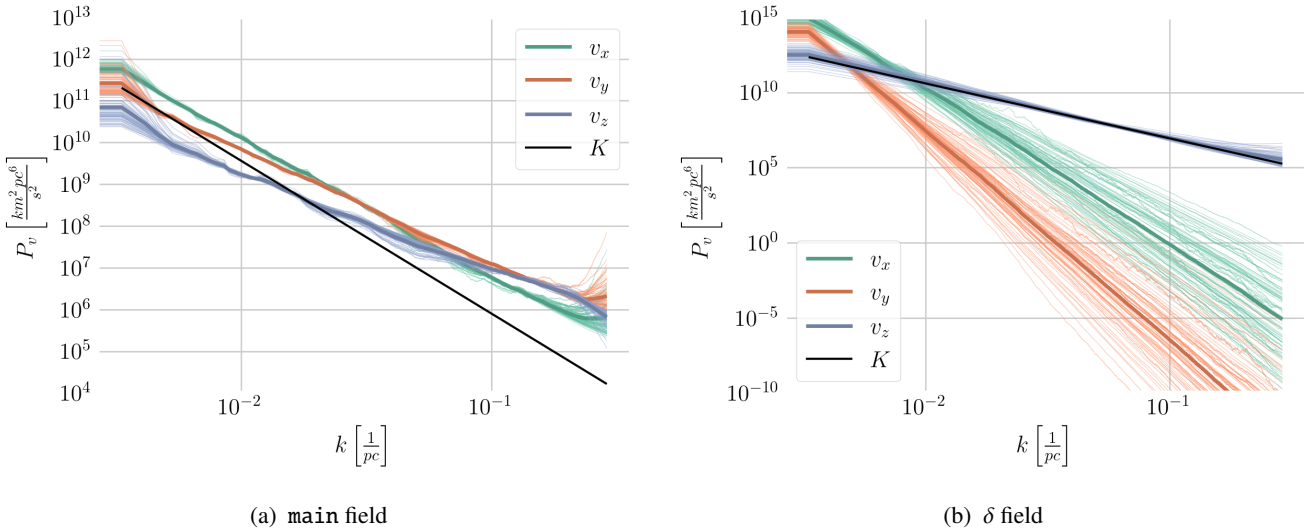


Fig. 4: The power spectra of the **main** and δ velocity field components, which are part of the forward model. The black line indicates the Kolmogorov slope $-11/3$, while the posterior samples are indicated as thin colored lines. We have scaled the line indicating the Kolmogorov spectrum to the average of the three component spectra at $k = 0.005 \text{ pc}^{-1}$ in each case, for illustrational purposes.

nificant structure. We note that the Kolmogorov slope implies scale invariance, but is not a clear-cut indicator for any physical process, be it random or ordered. Interestingly, the Kolmogorov value is found often in ISM-related fields, for instance, as the ‘Big power law in the sky’ (Armstrong et al. 1995; Chepurnov & Lazarian 2010; Hutschenreuter et al. 2024) in the diffuse plasma as measured over more than 12 orders of magnitude (Ferrière 2020) or Larson’s relation (Larson 1981), the dependence of the internal velocity dispersion of clouds on their size.

For the δ field fitting the systematic difference between the **main** and **secondary** fields, we find a very different picture, as shown in Fig. 4b. The z -component is completely consistent with a self-similar Kolmogorov spectrum, while the x - and y -fields are completely dominated by the lowest wavenumbers. This means that all additional small structure in the difference between the motions of the **secondary** and **main** is driven by a process that accelerates the younger stars downwards, consistent with our discussion in Sect. 4.1.

A 3D vector field also allows the calculation of two first-order differential fields, namely the divergence and the vorticity. The divergence of the **main** field is shown in Fig. 5, while the vorticity of the **main** field and both quantities for the **secondary** field are shown in Appendix H and online, all calculated via finite differences. The divergence indicates the tendency of the flow to contract (if it is negative) or expand (if it is positive). The vorticity gives the rate of rotation at a voxel, with positive values indicating right-handed rotation. Both quantities have the units of one over time, and can be interpreted as local measures of expansion rate and rotational frequency, respectively. The divergence plot in Fig. 5 shows strong small-scale fluctuations, which are a consequence of the derivatives boosting smaller scales. On average, it demonstrates the expanding nature of the Sco-Cen flow field as it is mostly positive throughout the volume. The contracting parts are mostly located within and in the direction of USco. The expansion rates per voxel have values up to a maximum of about 0.9 Myr^{-1} , with the more typical values being around 0.2 Myr^{-1} .

We show the divergence plot of the **secondary** and δ fields in Appendix H. Both show interesting features that can likely be

linked to recent feedback events; we again defer this analysis to future work.

Table 1: Marginal Posterior means of several characteristic values of the flow component fields and the absolute value fields, for \mathbf{V}_{main} , $\mathbf{V}_{\text{secondary}}$, and \mathbf{V}_{δ} .

	max km s ⁻¹	min km s ⁻¹	r.m.s. km s ⁻¹	p.s. slope unitless
$v_{\text{main},x}$	3.3 ± 0.2	-8.2 ± 0.1	1.97 ± 0.03	-3.1 ± 0.2
$v_{\text{main},y}$	8.4 ± 0.1	-3.4 ± 0.1	1.68 ± 0.03	-2.5 ± 0.1
$v_{\text{main},z}$	2.6 ± 0.1	-6.2 ± 0.1	1.05 ± 0.01	-2.5 ± 0.3
$ \mathbf{V}_{\text{main}} $	10.1 ± 0.1	0.2 ± 0.1	1.68 ± 0.02	N.A.
$v_{\text{sec},x}$	7.3 ± 0.7	-2.4 ± 0.4	1.71 ± 0.12	N.A.
$v_{\text{sec},y}$	9.4 ± 0.2	-1.3 ± 0.2	1.64 ± 0.03	N.A.
$v_{\text{sec},z}$	1.4 ± 0.3	-6.0 ± 0.2	1.04 ± 0.03	N.A.
$ \mathbf{V}_{\text{sec}} $	10.2 ± 0.2	1.0 ± 0.2	1.42 ± 0.06	N.A.
$v_{\delta,x}$	5.8 ± 0.7	-1.8 ± 0.7	1.31 ± 0.18	-10.3 ± 1.4
$v_{\delta,y}$	2.5 ± 0.2	-1.1 ± 0.2	0.65 ± 0.05	-14.0 ± 1.8
$v_{\delta,z}$	1.2 ± 0.2	-4.4 ± 0.2	0.83 ± 0.05	-3.7 ± 0.3
$ \mathbf{V}_{\delta} $	6.3 ± 0.4	0.4 ± 0.2	1.26 ± 0.14	N.A.

Notes. r.m.s. denotes the root mean square and p.s. the (unitless) power spectrum slope. The p.s. values are only shown if they are part of the forward model, otherwise no value (N.A.) is given.

5. Discussion

5.1. The driver of expansion

Inspecting the power spectra of the **main** field components in Fig. 4, we observe that the lines almost coincide at large wavenumbers k (i.e., small scales), with the x -component being somewhat damped, but significantly deviating at the largest scales, and with the z -component having almost a magnitude less power than the other two, especially compared to x . This reflects the fact that the large-scale expansion of Sco-Cen is mainly in the

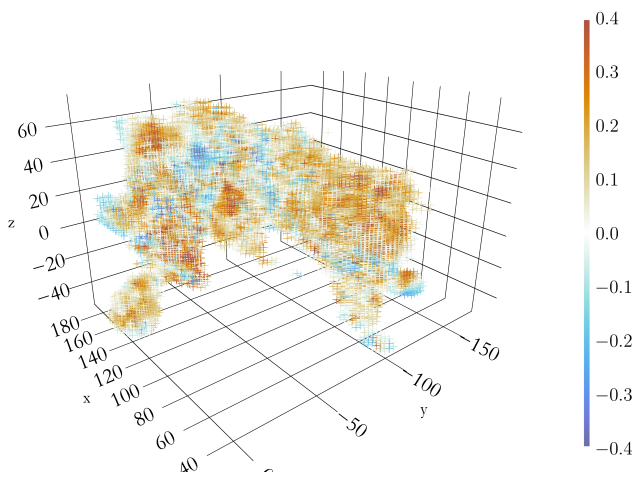


Fig. 5: Posterior mean of the divergence of the main flow field. A 3D interactive version of this plot is available [online](#).

Galactic plane, and also hints at Galactic rotation likely not being the main driver of the large-scale structure. In this case, one would expect a spherical structure to evolve in a slightly rotated ellipse (Palous et al. 1990), which implies that the y -spectrum should dominate over x and z at low k as it points towards Galactic rotation. This could be explained with initial conditions, but would require that the proto-Sco-Cen cloud was extremely stratified in the x -direction.

Inspecting the 3D scalar component fields (shown in Appendix G) corresponding to the spectra reveals a possible reason for the difference in power. The expected pattern from Palous et al. (1990) can be clearly seen in a top-down view of the field, which shows a clear large-scale gradient in velocities that could be readily fit with large k modes. In 3D, however, it becomes clear that the y -component has a structure that destroys this large-scale pattern to some degree, namely the LCC chain, which has a y -velocity opposite to its likely parent structure, the σ -Cen cluster. This indicates that feedback processes can dominate over Galactic rotation even at ages of 20 Myr and scales of up to 100 pc.

At small scales, the observed similarity in power may indicate that the additional power needed to depart from self-similarity stems from a small-scale process, which we conjecture to be stellar feedback. Here, we lack a good explanation for the somewhat damped spectrum in the x -component, as feedback is certainly isotropic on average. Since the x -direction is the one where RV-data matters the most due to the location of Sco-Cen with respect to the Sun, this might hint at missing small-scale structure in the data due to bad spatial RV sampling and relatively high noise in the RV data (see also the S/N analysis in Appendix A), but we cannot corroborate this conjecture.

If we take the picture of the evolution of Sco-Cen in the literature (R23a; R23b; P25; G25) at face value, we can connect the time domain with the phenomenology of the power spectra. Each feedback process injects energy at small scales, and the corresponding structure expands out as it ages, which is equivalent to moving to lower k in the power spectrum. We note that this proposed explanation is purely a memory effect reflecting the small-scale and localized energy injection, not a true inverse cascade which is observed numerically in, for example, ISM and cosmological magnetic fields (Brandenburg & Ntormousi 2023). This explains the lack of power at larger scales, which are diluted as there is no additional momentum input to offset spreading. We



have to mention that the amplification of smaller scales could, in principle, also be a consequence of an unresolved systematic effect in data, which, in case it is uncorrelated with the flow, would act as white noise in the spectrum and hence amplify smaller scales. The most likely culprit for this would be unresolved binarity in the RV data. While we cannot disprove this, we deem it unlikely to dominate the spectra, as this should affect the x and y components more, as these are more often aligned with the radial direction due to the relative location of the Sun to Sco-Cen.

In contrast, the fact that $v_{\delta,z}$ has a Kolmogorov spectrum may indicate that this is the result of a singular event that has injected momentum relatively recently, and that the aforementioned spreading effect of feedback-induced structures has not happened yet significantly. But we note that given the relatively small size of this sub-region compared to the resolution, it is unclear if this is a general result or a consequence of limited resolution.

We reiterate that the prior on the power spectrum is the same for all components, and specifically, the slope has a Gaussian prior centered on 7.3 with a standard deviation of 3.0. Since the slope is a log-log quantity, this prior is relatively constrained, hence indicating that this is a data-driven result. A caveat in the above discussion is that power spectra are averaged quantities. The fact that the secondary field has such a distinct correlation structure and the clear signature of feedback structures overlaying parts that might be driven by Galactic rotation might point towards the need to treat parts of Sco-Cen statistically separately depending on their substructure. This will be pursued in future work.

5.2. Flow substructure and origin

Figure 3 illustrates that the data harbors velocity structure that is not captured by cluster averages. Evidence for small scale kinematic structure was already given by Wright & Mamajek (2018), who interpreted this as indication that the OB association has not gone through a phase of dynamical relaxation. With reference to the SigMA clustering results, examples for this are significant sub-structure in the (rather extended) location of the σ -Cen cluster, velocity patterns within the isolated Cham 1 and 2 clusters, and a notable motion at the side of Sco-Cen facing the Galactic center, mostly traced by stars constituting the V1062-Sco, UPK 606, and Centaurus-far clusters. In general, the visual impression appears to indicate that these structures have originated from a similar feedback-driven mechanism as the cluster chains. The spatial arrangement of the acceleration patterns seen in the stellar flow field potentially indicates the evolution in structure, ranging from bulk motion in proto Sco-Cen, to radial expanding bulk flow, for instance, in USco, to clearly defined cluster chains to smaller low mass extensions, as, for example, traced by stars constituting the L134/183 cluster. This might indicate that the morphology of the flow largely depends on the mass of the material that has to be moved by the feedback sources.

A tentative but notable result is the location of the absolute minimum of the velocity field magnitude of the main field at $(x, y, z) = (85 \text{ pc}, -70 \text{ pc}, 19 \text{ pc})$, as this may indicate the origin of the flow. The position is very close but not coinciding (even when considering the error bars) with the geometric center of Sco-Cen as calculated by G25. We note that the location of this minimum depends on the choice of reference frame, and is hence far from settled. It is very difficult to reconcile the velocity center with any geometrically derived reference frame, as the flow center is located at the edge of stellar density that constitutes the plotting mask. It is, moreover, consistent with the on-sky loca-

tion of the origin of flow of diffuse matter in the ISM, which is very close to the Sun (i.e., several dozens of pc), as inferred by [Piecka et al. \(2024\)](#). This phenomenon may trace the oldest evolution history of Sco-Cen and may hint at anisotropic expansion of the proto-Sco-Cen cloud. We defer the quantitative analysis of this phenomenon to Paper II.

5.3. The evolution of stellar density

The typical divergence value of 0.2 Myr^{-1} can be taken as a characteristic rate of expansion, and we can use it to predict both the future and past density evolution of Sco-Cen to first order approximation using $\rho_t = \rho_0 e^{-\nabla V t}$. The typical stellar density of Sco-Cen is at about $0.1\text{--}0.2$ stars per pc^3 , hence, about $3\text{--}6$ stars per voxel (see Appendix C and Fig. A.3), while the background field is at about 0.1 stars per pc^3 . This implies that Sco-Cen will have largely diffused as an over-dense structure to the 10% level in about $11.5\text{--}15$ Myr and to the 1% level in about $23\text{--}26.5$ Myr. We note that clusters are typically identified as phase space over-densities (e.g., [Ratzenböck et al. 2023a; Hunt & Reffert 2023](#)), and that the kinematic structure of Sco-Cen might, in principle, allow for tracing it for longer (e.g., [Swiggum et al. 2024](#)).

Going back in time to the likely birth of the Sco-Cen association, 20 Myr ago, we arrive at initial density values of about $5\text{--}10$ stars per pc^3 for the values above. We note that in this regime, the projected density values are highly uncertain due to the exponential nature of the approximation; just doubling the divergence value already gives values between 300 and 600 stars per pc^3 , which interestingly lies in the same order of magnitude as the number of stars per pc^3 currently observed, e.g., in the Orion molecular cloud ([Herbig & Terndrup 1986; Hillenbrand & Hartmann 1998](#)). These numbers are first-order approximations and neither include models for the historical and ongoing star formation nor appreciate the much more complicated spatial structure of the flow. A detailed analysis of the history of Sco-Cen will be pursued in follow-up work.

5.4. Comparison to Cluster Chains

Cluster chains in Sco-Cen have been recently discovered and are linear alignments of young star clusters with gradients in age, velocity, and mass. They are interpreted as signatures of triggered star formation via stellar feedback and thought to represent a major component of Sco-Cen and its star formation history ([P23; P25; MR25](#)). We make use of these objects to study the systematic differences between clustering and field-based methods. Specifically, we analyze the CrA ([P23; P25](#)), LCC ([P25](#)), and TWA chains ([MR25](#)). In Fig. 6, we compare our analysis of the motion along the cluster chains with recently reported cluster velocities from the mentioned literature. We show both the projected and absolute values of the velocity field along the line segments that define the chains. All values, including the projections, are reported in the velocity frame of the respective reference publication. The comparison of the absolute values of the endpoints of our projections to the literature is not straightforward, as these values derived from clusters are averages over stellar populations, while we only plot the lines until the center of the respective clusters. Furthermore, the projection along a single line is an approximation, and the true chains are likely better described by chains of line segments. Smaller inconsistencies could also stem from the fact that we have used a slightly more extended RV-data set than [P23; P25; MR25](#).

In all cases, we confirm a positive velocity gradient of the component projected on the chain for most of the respective line segments. In the case of the CrA chain, the projection reveals that in the first part of the chain, which traverses the main body of Sco-Cen, the velocity field does not align with the linear projection. At about 25 pc from the start of the chain, the projected field is accelerated and up to about 80 pc is completely aligned with the full vector field, but experiences almost no acceleration. In the last 20 pc, the field is strongly accelerated. All in all, the CrA chain seems to have been boosted by two singular events, which seem to mirror the clustering results of [P23](#). The LCC chain, on the other hand, seems to be more continuously accelerated, with only a small plateau in its central part. Interestingly, the projected velocity component seems to have an almost constant offset to the absolute magnitude of the field, indicating that the full structure is moving relative to Sco-Cen independent of the internal acceleration. At last, the TWA chain, similarly to CrA, seems to experience acceleration in the beginning, where it is dominated by the internal structure of the σ -Cen cluster. After the projection leaves the cluster, the chain sees constant acceleration, interestingly again with an almost constant offset to the absolute magnitude. This is similar to the LCC chain, which is almost co-located in x and y position. There is a small deceleration happening at the end of the chain, which is not reported in [MR25](#), as it likely was lost in the cluster average. We note that this chain is much less sampled than the CrA and LCC chains, making the results more prone to outliers. We will defer a more detailed acceleration analysis to future work, not only along the chains but for the general flow field.

5.5. Comparison to CO

Only small parts of Sco-Cen are still harboring enough dense gas to produce significant, observable CO emission. [Tobin et al. \(2009\); Hacar et al. \(2016\); and Großschedl et al. \(2021\)](#) find that young stars that were recently born and which are still located close to their parent molecular cloud, as traced by CO, have not yet dynamically decoupled from the gas. The line-of-sight motions of these young stars (the RVs) are very similar to the gas RVs, at least in the first several 10^5 to a few million years after star-formation. We used the [Dame et al. \(2001\)](#) composite survey for the Ophiuchus and Lupus molecular clouds to derive first moment maps. To compare the stellar line of sight motions to CO, we used the [Edenhofer et al. \(2023\)](#) dust map to weight and integrate the radial component of the secondary velocity field, as this is the field constrained by the ρ -Oph, B59, and Lupus clusters, respectively. We converted the velocities to the local standard of rest frame (LSR) using the standard solar motion reported in [Ando et al. \(2011\)](#), and the procedure outlined in [Großschedl et al. \(2021\)](#) and [P23](#). This comparison relies on the idea that the dust in the [Edenhofer et al. \(2023\)](#) map traces the same quantity as the CO, which is likely only true to first order approximation.

We show a scatter plot between the first moment of the CO map and the dust-weighted integral of the secondary velocity field in the LSR frame in Fig. 7. The plot shows that the CO and velocity field moments show the same large-scale pattern; hence, more negative CO velocities correspond to more negative averaged field moments, albeit with significant scatter. But there is a clear offset between the two quantities, amounting to several km s^{-1} , with the CO almost consistently moving to more negative values, i.e., moving slower away from the LSR observer. We interpret this offset as ongoing decoupling between the stars and the gas, likely due to ongoing stellar feedback. We note that since

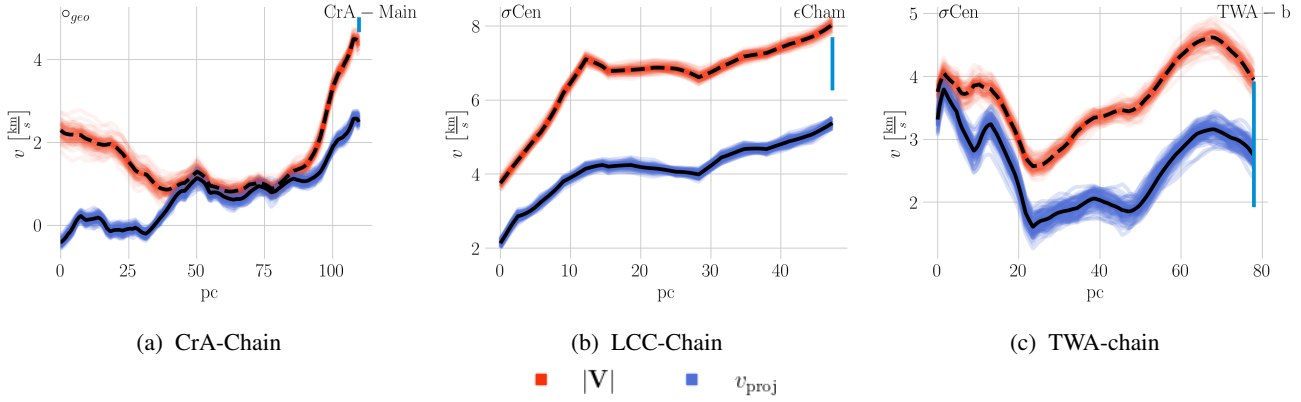


Fig. 6: Projected velocity profiles of the main velocity field in the reference frame of Posch et al. (2025) along the CrA, LCC, and TWA chains analyzed in P23; P25 and MR25. We note that in the case of the CrA chain, the starting point is the geometric center of Sco-Cen as defined in G25, while for the other two, it is the center of the σ -Cen cluster. The projection of the field onto the chain is shown in blue, while the absolute 3D magnitude is depicted in red. All quantities are accompanied by the respective posterior samples in lower opacity to illustrate uncertainties. We have included the values derived in the literature for the respective clusters at the end of the chains on the right of the plots as blue bars.

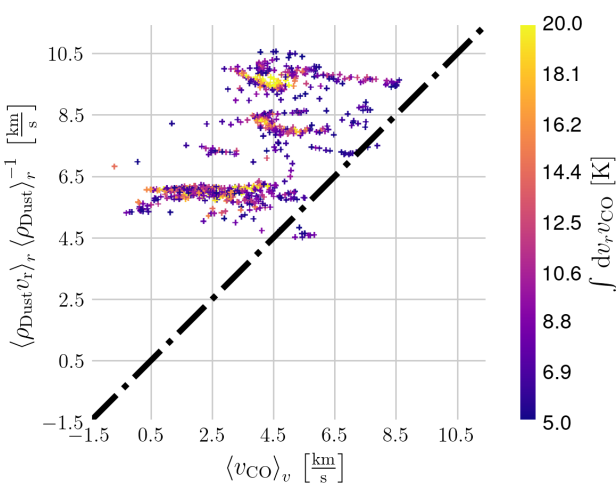


Fig. 7: Correlation between the first moment map (i.e., the mean over all velocity channels) and the dust-weighted line-of-sight integral of the RV field of the secondary field in the LSR frame, with integrated CO intensity color coded.

we lack stars embedded within the molecular clouds (which cannot be observed in *Gaia* due to high extinction), we lack the very young stars in our sample that might bridge this kinematic gap. Interestingly, the direction of the velocity offset indicates that the source of acceleration cannot come from the young clusters associated with the molecular clouds, as these are located mostly in front of the dense gas, relative to the LSR observer, and should hence accelerate the gas away from us. To account for the gas moving more slowly away from the LSR observer than the stars, it would take clusters located behind the gas as seen from the observer. We note that this is in line with the general trend in this part of Sco-Cen, already discussed in Sect. 4.1 and 4.2, which similarly sees a general downward motion compared to the main velocity field. We hence speculate that the source of feedback that causes this downward acceleration is still ongoing and is located above the secondary population and USco.

6. Conclusion

In this work, we present a method to infer the 3D flow field of stellar OB associations, and illustrate its capabilities by applying it to one of the closest young stellar associations, Sco-Cen. We reliably recover both qualitatively and quantitatively several features of the association already identified in the literature, such as the general inside-out acceleration pattern of the association and the cluster-chains connected to it. We demonstrate that the velocity field harbors significantly coherent structure below the scale of clusters.

One strength of a field-level picture is the easy accessibility of statistical descriptors, most importantly, the power spectrum. We demonstrate that the correlation structure of Sco-Cen has an excess in small-scale structure relative to a scale-invariant structure. This indicates that the observed expansion structure is likely driven at these small scales, which must be feedback processes. A stretching and acceleration due to Galactic rotation seems to be present, but is likely subdominant. Apart from structural insights, the field representation allows us to calculate derivative fields such as divergence and vorticity. These encode temporal expansion and rotation rates, and we have connected these to the history of Sco-Cen.

In this work, we mainly focus on the description of the method and a high-level description of the resulting maps, but only scratched the surface of what is possible in the analysis. In follow-up work, we will more deeply analyze the connection to ISM by deriving energy and momentum maps for the gas and dust fields in the region. We will furthermore analyze the acceleration structure of Sco-Cen in more detail, and deepen the analysis of the fluid characteristics of the field by calculating, e.g., the helicity density. Moreover, we aim to apply the method to further nearby star-forming regions such as Taurus, Perseus, Orion, and Vela OB2.

The largest limitation of our work stems from the RV data, both to the higher observational noise level as well as due to the higher likelihood of systematic biases stemming from, e.g., binaries. Both future data releases of ongoing surveys as well as newly developed instruments (e.g. Majewski et al. 2017; de Jong et al. 2012; Jin et al. 2024; Brown 2025) will help rem-

edy these issues, and potentially allow for a more detailed and better resolved reconstruction.

Acknowledgements. We would like to thank the referee for constructive comments. S.H. would like to thank Philipp Frank and Alena Rottensteiner for helpful discussions. Co-funded by the European Union (ERC, ISM-FLOW, 101055318). Views and opinions expressed are, however, those of the author(s) only and do not necessarily reflect those of the European Union or the European Research Council. Neither the European Union nor the granting authority can be held responsible for them. The computational results have been achieved using the Austrian Scientific Computing (ASC) infrastructure. JG acknowledges funding from the European Union, the Central Bohemian Region, and the Czech Academy of Sciences, as part of the MERIT fellowship (MSCA-COFUND Horizon Europe, Grant agreement 101081195). The following Python libraries were used in this work: `numpy` (Harris et al. 2020), `scipy` (Virtanen et al. 2020), `astropy` (Astropy Collaboration et al. 2022), `nifty` (Edenhofer et al. 2024), `findiff` (Baer 2018), `jax` (Bradbury et al. 2018), `jaxbind` (Roth et al. 2024), `cmasher` (van der Velden 2020), and `matplotlib` (Hunter 2007)

References

Abdurro'uf, Accetta, K., Aerts, C., et al. 2022, *ApJS*, 259, 35

Alves, J., Lombardi, M., & Lada, C. J. 2025, *A&A*, 697, A208

Ando, K., Nagayama, T., Omodaka, T., et al. 2011, *PASJ*, 63, 45

Armstrong, J. J., Tan, J. C., Wright, N. J., et al. 2025, *MNRAS*, 543, 2349

Armstrong, J. W., Rickett, B. J., & Spangler, S. R. 1995, *ApJ*, 443, 209

Arras, P., Frank, P., Haim, P., et al. 2022, *Nature Astronomy*, 6, 259

Arunima, A., Krumholz, M. R., Ireland, M. J., Zhang, C., & Hu, Z. 2025, *MNRAS*, 543, 358

Astropy Collaboration, Price-Whelan, A. M., Lim, P. L., et al. 2022, *ApJ*, 935, 167

Baer, M. 2018, `findiff` Software Package, <https://github.com/maroba/findiff>

Biazzo, K., Alcalá, J. M., Covino, E., et al. 2012, *A&A*, 547, A104

Blaauw, A. 1946, Publications of the Kapteyn Astronomical Laboratory Groningen, 52, 1

Blaauw, A. 1964, *ARA&A*, 2, 213

Bradbury, J., Frostig, R., Hawkins, P., et al. 2018, *JAX*: composable transformations of Python+NumPy programs

Brandenburg, A. & Ntormousi, E. 2023, *ARA&A*, 61, 561

Breitschwerdt, D., Feige, J., Schulreich, M. M., et al. 2016, *Nature*, 532, 73

Briceño-Morales, G. & Chanamé, J. 2023, *MNRAS*, 522, 1288

Brown, A. G. A. 2025, arXiv e-prints, arXiv:2503.01533

Buder, S., Sharma, S., Kos, J., et al. 2021, *MNRAS*, 506, 150

Castro-Ginard, A., Penoyre, Z., Casey, A. R., et al. 2024, *A&A*, 688, A1

Chen, C. H., Mamajek, E. E., Bitner, M. A., et al. 2011, *ApJ*, 738, 122

Chepurnov, A. & Lazarian, A. 2010, *ApJ*, 710, 853

Chevance, M., Krumholz, M. R., McLeod, A. F., et al. 2023, in *Astronomical Society of the Pacific Conference Series*, Vol. 534, *Protostars and Planets VII*, ed. S. Inutsuka, Y. Aikawa, T. Muto, K. Tomida, & M. Tamura, 1

Dahm, S. E., Slesnick, C. L., & White, R. J. 2012, *ApJ*, 745, 56

Dame, T. M., Hartmann, D., & Thaddeus, P. 2001, *ApJ*, 547, 792

Damiani, F., Prisinzano, L., Pillitteri, I., Micela, G., & Sciortino, S. 2019, *A&A*, 623, A112

de Bruijne, J. H. J. 1999, *MNRAS*, 310, 585

de Geus, E. J. 1992, *A&A*, 262, 258

de Geus, E. J., de Zeeuw, P. T., & Lub, J. 1989, *A&A*, 216, 44

de Jong, R. S., Bellido-Tirado, O., Chiappini, C., et al. 2012, in *Society of Photo-Optical Instrumentation Engineers (SPIE) Conference Series*, Vol. 8446, *Ground-based and Airborne Instrumentation for Astronomy IV*, ed. I. S. McLean, S. K. Ramsay, & H. Takami, 84460T

De Silva, G. M., Freeman, K. C., Bland-Hawthorn, J., et al. 2015, *MNRAS*, 449, 2604

Edenhofer, G., Alves, J., Zucker, C., Posch, L., & Enßlin, T. A. 2024, *A&A*, 687, L9

Edenhofer, G., Frank, P., Roth, J., et al. 2024, *Journal of Open Source Software*, 9, 6593

Edenhofer, G., Zucker, C., Frank, P., et al. 2023, *A Parsec-Scale Galactic 3D Dust Map out to 1.25 kpc from the Sun*

Enßlin, T. A. 2019, *Annalen der Physik*, 531, 1800127

Fang, M., Pascucci, I., Edwards, S., et al. 2023, *ApJ*, 945, 112

Ferrière, K. 2020, *Plasma Physics and Controlled Fusion*, 62, 014014

Forbes, J. C., Alves, J., & Lin, D. N. C. 2021, *Nature Astronomy*, 5, 1009

Frank, P., Leike, R., & Enßlin, T. A. 2021, *Entropy*, 23, 853

Frasca, A., Biazzo, K., Alcalá, J. M., et al. 2017, *A&A*, 602, A33

Frisch, P. C. 1995, *Space Sci. Rev.*, 72, 499

Fuchs, B., Breitschwerdt, D., de Avillez, M. A., Dettbarn, C., & Flynn, C. 2006, *MNRAS*, 373, 993

Gaia Collaboration, Vallenari, A., Brown, A. G. A., et al. 2023, *A&A*, 674, A1

Galli, P. A. B., Bertout, C., Teixeira, R., & Ducourant, C. 2013, *A&A*, 558, A77

Gilmore, G., Randich, S., Asplund, M., et al. 2012, *The Messenger*, 147, 25

Gontcharov, G. A. 2006, *Astronomy Letters*, 32, 759

Großschedl, J. E., Alves, J., Meingast, S., & Herbst-Kiss, G. 2021, *A&A*, 647, A91

Großschedl, J. E., Alves, J., Ratzenböck, S., et al. subm., *A&A*, arXiv:2509.19487

Guenther, E. W., Esposito, M., Mundt, R., et al. 2007, *A&A*, 467, 1147

Hacar, A., Alves, J., Forbrich, J., et al. 2016, *A&A*, 589, A80

Harju, J., Haikala, L. K., Mattila, K., et al. 1993, *A&A*, 278, 569

Harris, C. R., Millman, K. J., van der Walt, S. J., et al. 2020, *Nature*, 585, 357

Herbig, G. H. & Terndrup, D. M. 1986, *ApJ*, 307, 609

Hillenbrand, L. A. & Hartmann, L. W. 1998, *The Astrophysical Journal*, 492, 540

Hunt, E. L. & Reffert, S. 2023, *A&A*, 673, A114

Hunter, J. D. 2007, *Computing in Science & Engineering*, 9, 90

Hutschenreuter, S., Anderson, C. S., Betti, S., et al. 2022, *A&A*, 657, A43

Hutschenreuter, S., Haverkorn, M., Frank, P., Raycheva, N. C., & Enßlin, T. A. 2024, *A&A*, 690, A314

Jackson, R. J., Jeffries, R. D., Wright, N. J., et al. 2022, *MNRAS*, 509, 1664

James, D. J., Melo, C., Santos, N. C., & Bouvier, J. 2006, *A&A*, 446, 971

Jilinski, E., Daflon, S., Cunha, K., & de La Reza, R. 2006, *A&A*, 448, 1001

Jin, S., Trager, S. C., Dalton, G. B., et al. 2024, *MNRAS*, 530, 2688

Joergens, V. & Guenther, E. 2001, *A&A*, 379, L9

Kapteyn, J. C. 1914, *ApJ*, 40, 43

Katz, D., Sartoretti, P., Guerrier, A., et al. 2023, *A&A*, 674, A5

Krause, M. G. H., Burkert, A., Diehl, R., et al. 2018, *A&A*, 619, A120

Kunder, A., Kordopatis, G., Steinmetz, M., et al. 2017, *AJ*, 153, 75

Larson, R. B. 1981, *MNRAS*, 194, 809

Leike, R. H. & Enßlin, T. A. 2019, *A&A*, 631, A32

Leike, R. H., Glatzle, M., & Enßlin, T. A. 2020, *A&A*, 639, A138

Loren, R. B. 1989, *ApJ*, 338, 902

Luhman, K. L. 2022, *The Astronomical Journal*, 163, 24

Majewski, S. R., Schiavon, R. P., Frinchaboy, P. M., et al. 2017, *AJ*, 154, 94

Makarov, V. V. 2007a, *ApJ*, 670, 1225

Makarov, V. V. 2007b, *ApJS*, 169, 105

McKee, C. F. & Ostriker, E. C. 2007, *Annual Review of Astronomy and Astrophysics*, 45, 565

Miret-Roig, N., Alves, J., Ratzenböck, S., et al. 2025, *A&A*, 694, A60

Miret-Roig, N., Galli, P. A. B., Olivares, J., et al. 2022, *A&A*, 667, A163

Murphy, S. J., Lawson, W. A., & Bessell, M. S. 2013, *MNRAS*, 435, 1325

Nehmé, C., Gry, C., Boulanger, F., et al. 2008, *A&A*, 483, 471

Neuhäuser, R., Gießler, F., & Hambaryan, V. V. 2020, *MNRAS*, 498, 899

Nguyen, D. C., Brandeker, A., van Kerwijk, M. H., & Jayawardhana, R. 2012, *ApJ*, 745, 119

Oppermann, N., Junklewitz, H., Robbers, G., et al. 2012, *A&A*, 542, A93

Palous, J., Franco, J., & Tenorio-Tagle, G. 1990, *A&A*, 227, 175

Pecaut, M. J. & Mamajek, E. E. 2016, *MNRAS*, 461, 794

Piecka, M., Hutschenreuter, S., & Alves, J. 2024, *A&A*, 689, A84

Piecka, M., Posch, L., Meingast, S., et al. 2025, *A&A*, 702, L1

Pöppel, W. G. L., Bajaja, E., Arnal, E. M., & Morras, R. 2010, *A&A*, 512, A83

Posch, L., Alves, J., Miret-Roig, N., et al. 2025, *A&A*, 693, A175

Posch, L., Miret-Roig, N., Alves, J., et al. 2023, *A&A*, 679, L10

Queiroz, A. B. A., Anders, F., Santiago, B. X., et al. 2018, *MNRAS*, 476, 2556

Quintana, A. L. 2024, arXiv e-prints, arXiv:2412.10769

Ratzenböck, S., Großschedl, J. E., Alves, J., et al. 2023b, *A&A*, 678, A71

Ratzenböck, S., Großschedl, J. E., Möller, T., et al. 2023a, *A&A*, 677, A59

Redfield, S. & Linsky, J. L. 2008, *ApJ*, 673, 283

Robitaille, J. F., Scaife, A. M. M., Carretti, E., et al. 2018, *A&A*, 617, A101

Roth, J., Reinecke, M., & Edenhofer, G. 2024, *Journal of Open Source Software*, 9, 6532

Rybicki, J., Green, G. M., Rix, H.-W., et al. 2022, *MNRAS*, 510, 2597

Sacco, G. G., Spina, L., Randich, S., et al. 2017, *A&A*, 601, A97

Santana, F. A., Beaton, R. L., Covey, K. R., et al. 2021, *AJ*, 162, 303

Scheel-Platz, L. I., Knollmüller, J., Arras, P., et al. 2023, *A&A*, 680, A2

Söding, L., Edenhofer, G., Enßlin, T. A., et al. 2025, *A&A*, 693, A139

Steinmetz, M., Matijević, G., Enke, H., et al. 2020a, *AJ*, 160, 82

Stiskalek, R., Desmond, H., Devriendt, J., et al. 2025, *MNRAS* arXiv:2502.00121

Swiggum, C., Alves, J., Benjamin, R., et al. 2024, *Nature*, 631, 49

Tobin, J. J., Hartmann, L., Furesz, G., Mateo, M., & Megeath, S. T. 2009, *ApJ*, 697, 1103

Torres, C. A. O., Quast, G. R., da Silva, L., et al. 2006, *A&A*, 460, 695

Truelove, J. K. & McKee, C. F. 1999, *ApJS*, 120, 299

van der Velden, E. 2020, *The Journal of Open Source Software*, 5, 2004

Virtanen, P., Gommers, R., Oliphant, T. E., et al. 2020, *Nature Methods*, 17, 261

Westerkamp, M., Eberle, V., Guardiani, M., et al. 2024, *A&A*, 684, A155

Wichmann, R., Covino, E., Alcalá, J. M., et al. 1999, *MNRAS*, 307, 909

Wright, N. J. & Mamajek, E. E. 2018, *MNRAS*, 476, 381

Zucker, C., Alves, J., Goodman, A., Meingast, S., & Galli, P. 2023, in *Astronomical Society of the Pacific Conference Series*, Vol. 534, *Protostars and Planets VII*, ed. S. Inutsuka, Y. Aikawa, T. Muto, K. Tomida, & M. Tamura, 43

Zucker, C., Goodman, A., Alves, J., et al. 2021, *ApJ*, 919, 35

Zucker, C., Goodman, A. A., Alves, J., et al. 2022, *Nature*, 601, 334

Table A.1: Overview of the clusters in the **main** selection.

SigMA name	N_{stars}	age [Myr]
Antares	502	$12.7^{+0.4}_{-1.3}$
ρ Sco	240	$13.7^{+1.3}_{-0.6}$
Scorpio-Body	373	$14.7^{+0.8}_{-0.7}$
US-foreground	276	$19.1^{+2.4}_{-1.3}$
V1062-Sco	1029	$15.0^{+0.9}_{-1.4}$
μ Sco	54	$17.2^{+0.9}_{-2.4}$
Libra-South	71	$20.0^{+2.5}_{-2.2}$
η Lup	769	$15.3^{+0.6}_{-0.3}$
ϕ Lup	1114	$16.9^{+0.9}_{-0.6}$
e Lup	516	$20.9^{+0.7}_{-0.8}$
UPK606	131	$13.4^{+1.0}_{-0.7}$
ρ Lup	246	$14.4^{+0.4}_{-0.9}$
ν Cen	1737	$15.7^{+0.3}_{-0.9}$
σ Cen	1805	$15.5^{+0.6}_{-0.5}$
Crux	394	$11.2^{+1.0}_{-1.0}$
Musca-foreground	95	$10.2^{+1.0}_{-0.7}$
ϵ Cham	39	$8.8^{+0.6}_{-0.4}$
η Cham	30	$9.4^{+1.4}_{-0.9}$
Pipe-North	42	$15.9^{+1.6}_{-2.1}$
θ Oph	98	$15.4^{+0.8}_{-1.9}$
CrA-Main	96	$8.5^{+2.0}_{-2.4}$
CrA-North	351	$11.6^{+0.5}_{-0.6}$
Scorpio-Sting	132	$14.5^{+0.6}_{-0.6}$
Centaurus-Far	99	$8.5^{+1.1}_{-1.3}$
Chamaeleon-1	192	$3.8^{+1.9}_{-0.9}$
Chamaeleon-2	54	$2.8^{+0.7}_{-0.9}$
L134/L183	24	$9.6^{+1.7}_{-2.2}$

Appendix A: Further details on the data

Table A.2: Overview of the clusters in the **secondary** selection.

SigMA name	N_{stars}	age [Myr]
B59	32	$3.4^{+3.1}_{-0.9}$
β -Sco	285	$7.6^{+0.8}_{-0.7}$
δ -Sco	691	$9.8^{+1.2}_{-1.4}$
ν -Sco	150	$5.8^{+1.8}_{-0.5}$
σ -Sco	544	$10.0^{+1.0}_{-0.5}$
ρ -Oph/L1688	535	$3.8^{+0.4}_{-0.4}$
Lupus-1-4	226	$6.0^{+0.6}_{-0.9}$
L134/L138	24	$9.6^{+1.7}_{-2.2}$

We use the RV compilation from [G25](#), who collected the data from the following 23 spectral surveys or literature catalogs: [Wichmann et al. \(1999\)](#); [Joergens & Guenther \(2001\)](#); [Torres et al. \(2006\)](#); [Gontcharov \(2006\)](#); [Jilinski et al. \(2006\)](#); [James et al. \(2006\)](#); [Guenther et al. \(2007\)](#); [Chen et al. \(2011\)](#); [Biazzo et al. \(2012\)](#); [Dahm et al. \(2012\)](#); [Nguyen et al. \(2012\)](#); [Gilmore et al. \(2012\)](#); [Galli et al. \(2013\)](#); [De Silva et al. \(2015\)](#);

Table A.3: The prior hyper-parameters for the correlation structure model of the v_x , v_y , v_z components of **main** and δ vector fields.

Parameter Name	Unit	main	δ
offset mean x	km s^{-1}	-6.7	0
offset mean y	km s^{-1}	-19.7	0
offset mean z	km s^{-1}	-5.5	0
offset std* (x, y, z)	km s^{-1}	15 ± 15	
fluctuations* (x, y, z)	km s^{-1}	25 ± 25	
loglogavgslope (x, y, z)		-7.3 ± 3.0	
asperity* (x, y, z)		0.5 ± 0.5	
flexibility* (x, y, z)		0.5 ± 0.5	

Notes. The parameters marked with a * have log-normal priors, with the given mean and standard deviations moment matched to the log-normal distribution. Units are given if the prior is applicable; otherwise, the quantities are unitless. The prior is the same for both fields, apart from the three offset mean parameters.

[Murphy et al. \(2013\)](#); [Majewski et al. \(2017\)](#); [Sacco et al. \(2017\)](#); [Kunder et al. \(2017\)](#); [Frasca et al. \(2017\)](#); [Buder et al. \(2021\)](#); [Santana et al. \(2021\)](#); [Steinmetz et al. \(2020a\)](#); [Miret-Roig et al. \(2022\)](#); [Abdurro'uf et al. \(2022\)](#); [Jackson et al. \(2022\)](#); [Katz et al. \(2023\)](#); [Fang et al. \(2023\)](#); [Miret-Roig et al. \(2025\)](#).

In Fig. A.1 we show the S/N of the used proper motion and RV data. This illustrates the high quality of the proper motion data compared to the radial velocities.

Figure A.2 illustrates the likelihood $\mathcal{P}_{\text{voxel}}$ (as color-scale) for each star, highlighting the probability of the star being the voxel it falls into if using the inverted parallax as a distance estimator. The strong heterogeneity of the parallax uncertainty leads to $\mathcal{P}_{\text{voxel}}$ values of almost 0 to almost 1 (i.e., the star is almost certainly in the respective voxel).

We do not include the clusters labeled ‘Norma-North’, ‘Ophiuchus-North-Far’, and ‘Ophiuchus-South-East’ from [R23a](#), as they are likely not connected to the Sco-Cen OB association, but interlopers from adjacent regions based on their kinematic and age properties, following also the analyses of [R23b](#) and [G25](#). The clusters in the **main** and **secondary** selection are summarized in Table A.1 and Table A.2, respectively, including their ages and the number of stars contained in each cluster.

Appendix B: Physical field assumption

In fitting a flow field to the observed 3D space motion of stars, we take an analogy to fluid dynamics where continuous fields describe the discrete motion of particles with dynamics governed by the continuity equation. This comes with several implied assumptions, which we try to make explicit in this section.

The first is the continuum hypothesis and the associated notion of smoothness, i.e., the idea that neighboring volume elements will have similar field values, which is an important ingredient to our prior model. While the degree of smoothness is uncertain and a global free parameter of the model, it can never be absent, as this is the only way to regularize the many parameters. Since we work on a discretized grid, we assume that typical structures of the field will have dimensions larger than the voxel size of 3 pc.

Furthermore, the stellar flow is likely inviscid (since star-star interactions are negligible). The lack of viscosity implies that

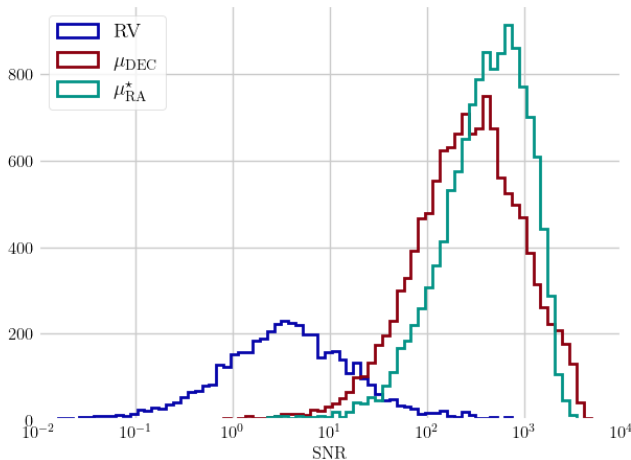


Fig. A.1: Illustrating the quality of the used data sets, as traced by the S/N, i.e., the ratio of data value over observational errors.

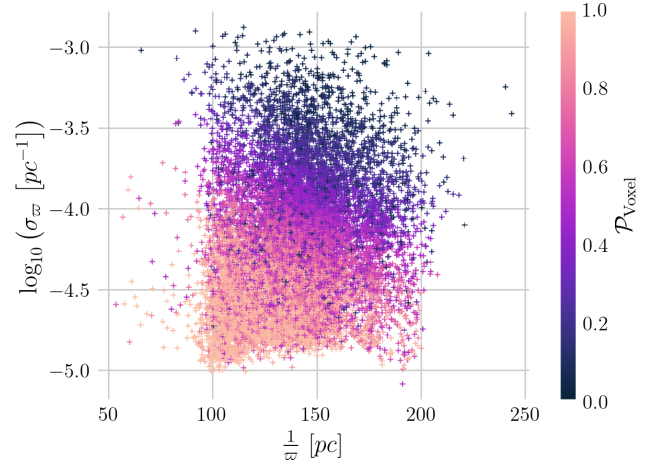


Fig. A.2: Scatter plot of observed distance as derived from $1/\tau$ vs. the errors on τ . Color-coded is the likelihood of the stars to actually be in the voxel where they are found, according to our grid definition and the τ noise statistics.

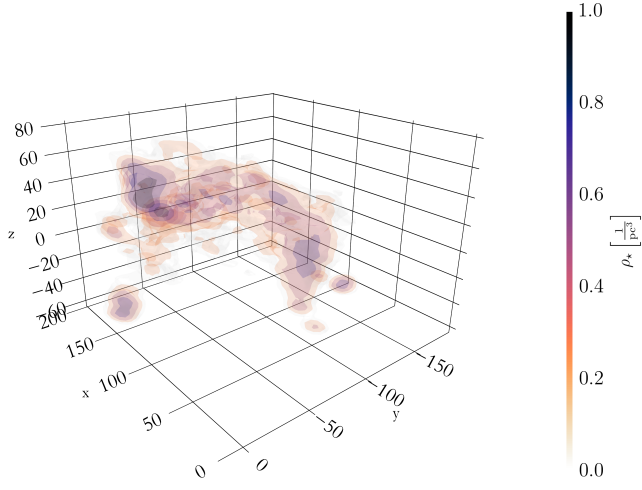


Fig. A.3: Stellar density of the SigMA selection of stars in Sco-Cen. A 3D interactive version of this plot is available [online](#).

stellar flows can overlap easily, in which case a single flow field would at best describe the net flow between volume elements. In this case, the field would lose much of its descriptive value as derived quantities such as energy or momentum densities become meaningless, as they only make sense in the absence of co-spatiality of flows. This can be remedied by introducing more flow components to the model.

Appendix C: Stellar density

We show a kernel density estimation of the stellar number density field in Fig. A.3. This field was calculated using the mean Cartesian positions as input to `scipy.stats.gaussian_kde` function in python, with the `bw_method` parameter set to 0.1. The main purpose of this field is the definition of the boundaries of Sco-Cen for visualization; we have refrained from incorporating parallax uncertainties in the estimation. In future work, the

calculation of, e.g., a stellar momentum field will require dealing with this source of uncertainty.

Appendix D: Prior

All three components of both the `main` and δ vector fields are modeled as Gaussian random fields with unknown correlation structure, using the model by [Arras et al. \(2022\)](#). The hyper-parameters are listed in Table A.3. These describe the prior assumptions for the correlation structure of Gaussian random fields representing the three velocity components (v_x, v_y, v_z) of the `main` and `add` vector fields in the barycentric velocity frame. The ‘offset’ parameters specify the expected value of the global mean of the component fields, where the `main` field shows a significant non-zero prior offset centered on the [G25](#) reference frame, while the `add` field is centered at zero. The ‘offset std’ reflects the prior uncertainty around the offset mean, and is set uniformly across components at $15 \pm 15 \text{ km s}^{-1}$, implying a broad and weakly informative prior that encompasses the frame difference between the barycenter and Sco-Cen. The ‘fluctuations’ term models the standard deviation of the variations around the mean, also set with a wide uncertainty band of $25 \pm 25 \text{ km s}^{-1}$, capturing the magnitude of random local deviations, and easily covering the expected velocity range of Sco-Cen (e.g., [G25](#)).

The remaining parameters shape the spectral behavior of the Gaussian random fields. ‘`loglogavgslope`’ determines the slope of the power spectrum in log-log space, with steeper slopes correspond to smoother fields. We choose a rather smooth a-prior value of 7.3, with a standard deviation of 3, chosen such that a wide range of slope values is covered within the $1-\sigma$ bound. ‘`asperity`’ controls the degree of spikiness in deviations from the power-law, while ‘`flexibility`’ regulates the amplitude of these variations. Both are given non-informative priors centered at 0.5 with wide uncertainties of 0.5, reflecting agnosticism about how structured or smooth the power spectra might be. Together, these parameters define a flexible yet physically plausible model for the underlying spatial structure in the vector fields, following the hierarchical approach of [Arras et al. \(2022\)](#).

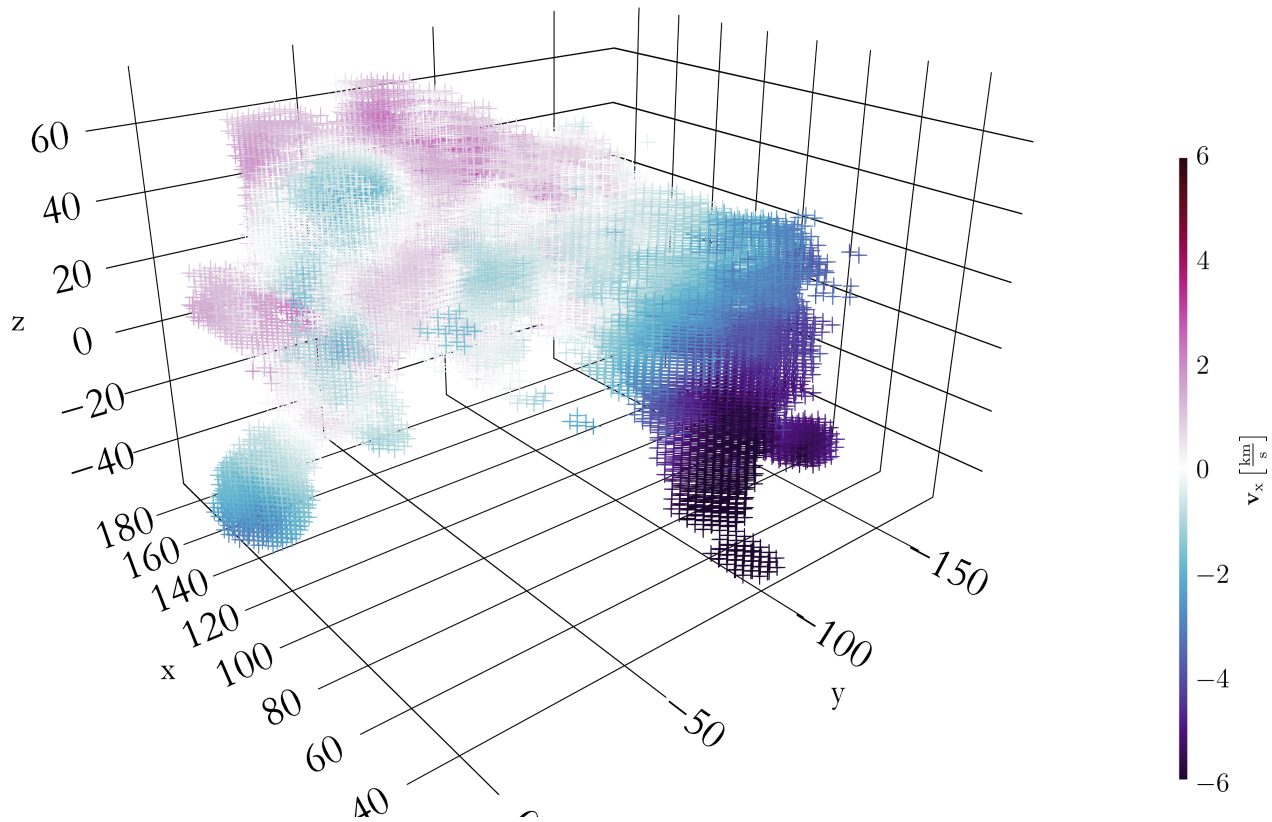


Fig. A.4: Posterior mean x-component main flow field. A 3D interactive version of this plot is available [online](#).

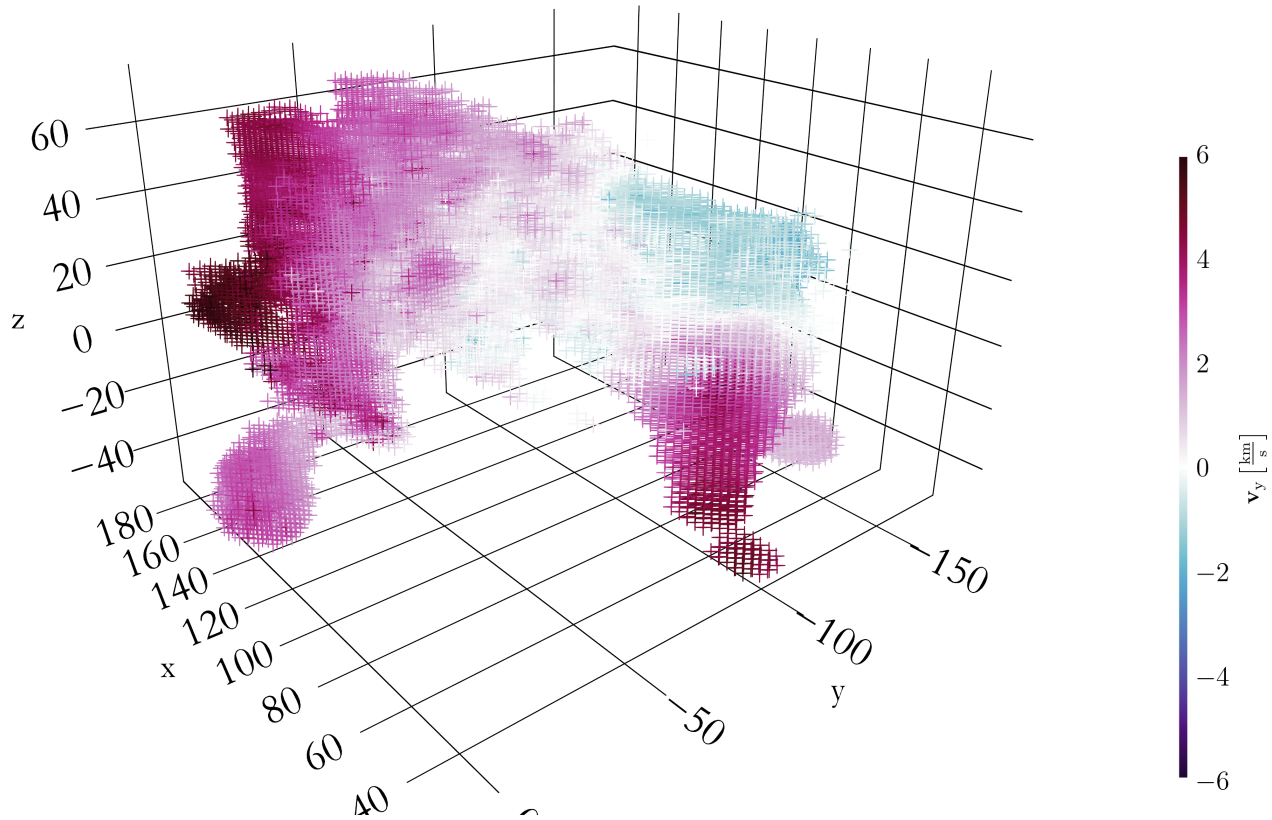


Fig. A.5: Posterior mean y-component main flow field. A 3D interactive version of this plot is available [online](#).

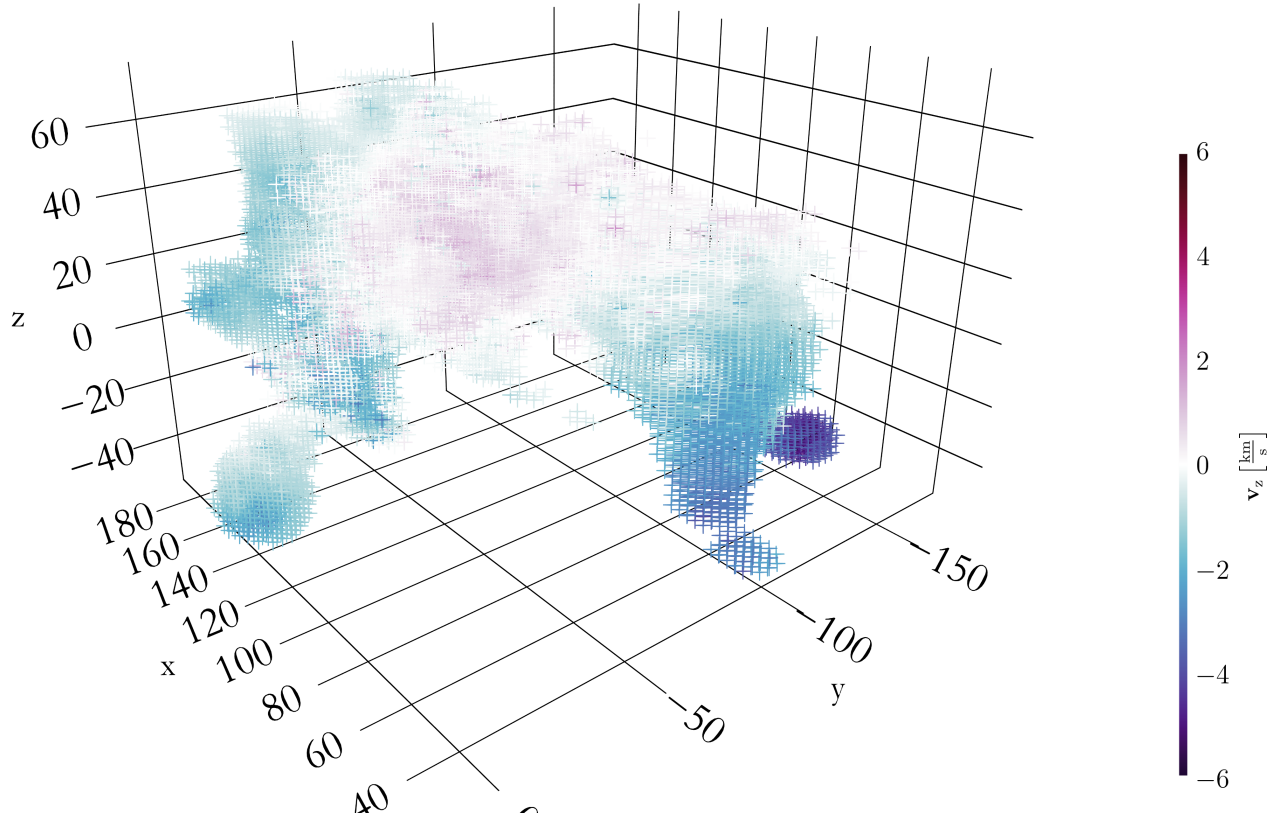


Fig. A.6: Posterior mean z-component main flow field. A 3D interactive version of this plot is available [online](#).

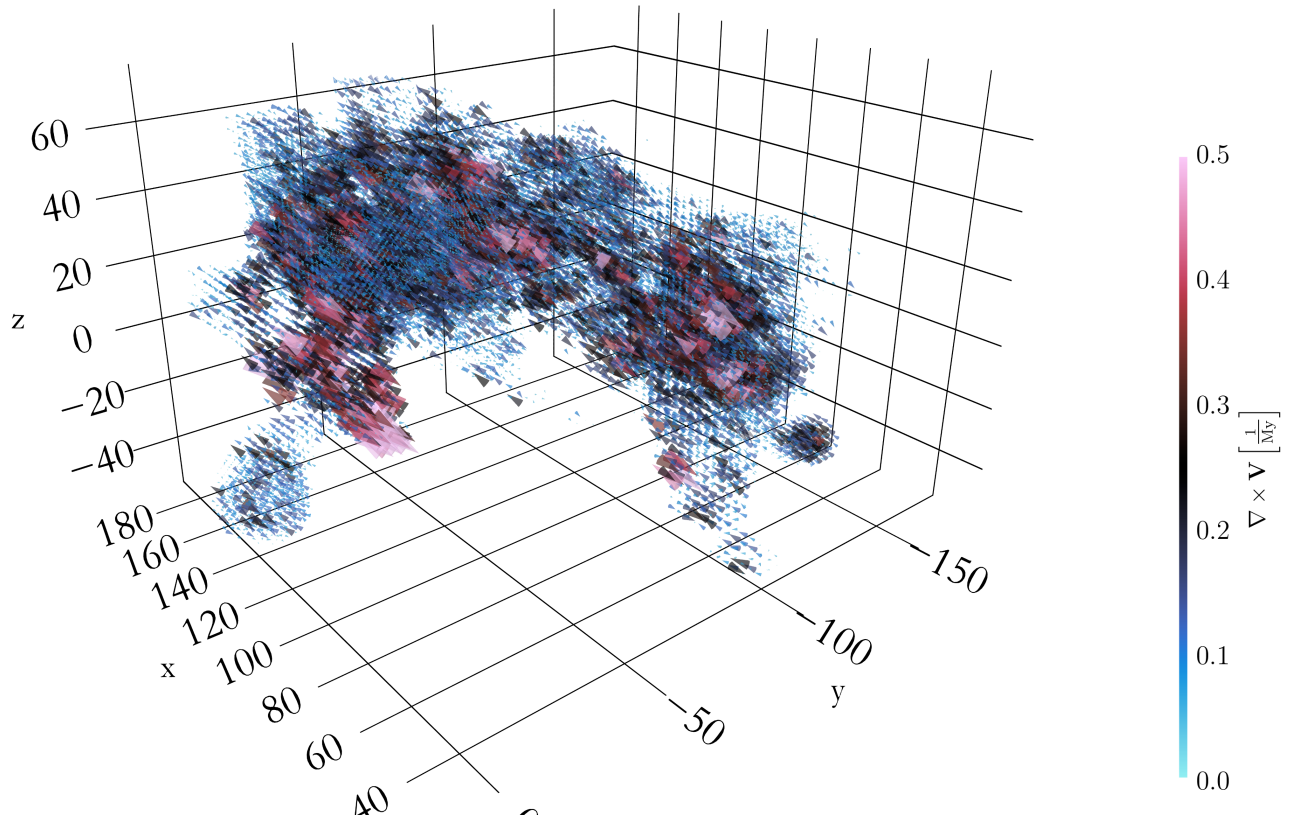


Fig. A.7: Posterior mean vorticity of the main flow field. A 3D interactive version of this plot is available [online](#).

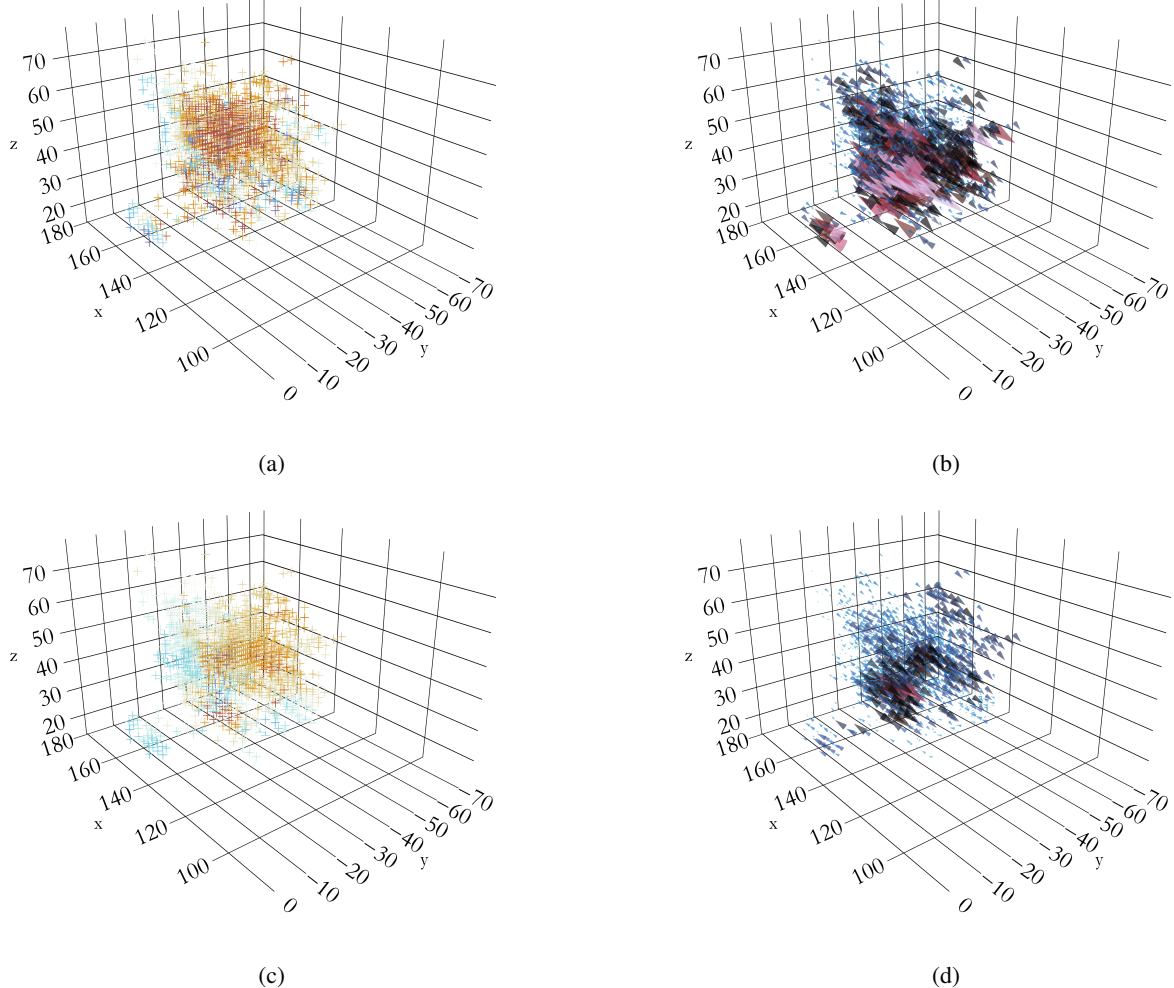


Fig. A.8: Posterior mean divergence vorticity of the secondary and δ flow fields. The colormaps in these plots are the same as in the respective main field plots. 3D interactive versions of these plots are available [online](#).

Appendix E: Details on the likelihood derivation

Here we explicitly outline several calculation steps that were omitted in the description of the likelihood in Sect. 3.3.3. We focus on a subset of stars with unobserved RVs and uncertain distance estimates, since this case allows us to demonstrate the necessary steps while still allowing for a more compact notation. The case including RVs is completely analogous. A large part of this calculation follows roughly similar approaches as in Leike & Enßlin (2019) and Edenhofer et al. (2023) and is quite general.

Following the notation laid out in Sect. 3, we denote the likelihood variables, in this case the proper motion data set, as μ , and the observed parallaxes as ϖ . To connect the velocity field and data in the following calculation, we introduce the true proper motions

$$\tilde{\mu} = \mu_{\star}(\mathbf{V}, \tilde{\varpi}) \quad (E.1)$$

i.e. the true velocity field \mathbf{V} evaluated at the true distances $1/\tilde{\varpi}$. The true proper motions and parallaxes are related to the data via

$$\mu = \tilde{\mu} + n_{\mu} = \mu_{\star}(\mathbf{V}, \tilde{\varpi}) + n_{\mu} \quad (E.2)$$

$$\varpi = \tilde{\varpi} + n_{\varpi}, \quad (E.3)$$

with correlated noise terms n_{μ} and n_{ϖ} , with observational covariance $C_{\mu, \varpi}$. Expanding the likelihood in all of the (unknown)

quantities introduced in Eqs. (E.1), (E.2), and (E.3) gives:

$$\begin{aligned} \mathcal{P}(\mu | \mathbf{V}, \varpi, C_{\mu, \varpi}) &= \\ &= \int d\tilde{\varpi} dn_{\mu} dn_{\varpi} \mathcal{P}(\mu, \tilde{\varpi}, n_{\mu}, n_{\varpi} | \mathbf{V}, \varpi, C_{\mu, \varpi}) = \\ &= \int d\tilde{\varpi} dn_{\mu} dn_{\varpi} \mathcal{P}(\mu | \mathbf{V}, \tilde{\varpi}, n_{\mu}) \mathcal{P}(\tilde{\varpi}, n_{\mu}, n_{\varpi} | \mathbf{V}, \varpi, C_{\mu, \varpi}) = \\ &\text{and similarly using Eq. (E.3) for the parallaxes} \\ &= \int d\tilde{\varpi} dn_{\mu} dn_{\varpi} \mathcal{P}(\mu | \mathbf{V}, \tilde{\varpi}, n_{\mu}) \mathcal{P}(\tilde{\varpi} | n_{\varpi}, \varpi) \mathcal{P}(n_{\mu}, n_{\varpi} | C_{\mu, \varpi}) \end{aligned} \quad (E.4)$$

Since the only information we have on the noise statistics is the covariance, the appropriate noise prior distribution to choose is a bi-variate zero-centered Gaussian. This distribution maximizes the information entropy in case one only has information on the first and second moments, i.e., it makes the least additional assumptions (Enßlin 2019). The first two distributions are delta

distributions, since they are completely determined by Eqs. (E.2) and (E.3). This allows us to perform the marginalization over the noise terms analytically, giving us

$$\mathcal{P}(\mu|V, \varpi, C_{\mu, \varpi}) = \int d\tilde{\varpi} \mathcal{G}\left(\frac{\mu - \mu_{\star}(V, \tilde{\varpi})}{\tilde{\varpi} - \varpi}, C_{\varpi, \mu}\right) \quad (\text{E.5})$$

The final step, namely the marginalization over $\tilde{\varpi}$, is not analytically tractable in general, since the variation of μ_{\star} with distance depends on the unknown structure of the velocity field along the line of sight. We hence introduce the following numerical approximation

$$\begin{aligned} \mathcal{P}(\mu|V, \varpi, C_{\mu, \varpi}) &= \int d\tilde{\varpi} \mathcal{P}(\mu, \tilde{\varpi}|V, \varpi, C_{\mu, \varpi}) \\ &\approx \sum_i \mathcal{P}(\mu|\tilde{\varpi}_i, V, \varpi, C_{\mu, \varpi}) \\ &\approx \mathcal{G}(\mu - \langle \mu_{\star} \rangle_{\varpi}, C_{\mu} + \langle C_{\mu} \rangle_{\varpi}) \end{aligned} \quad (\text{E.6})$$

with

$$\langle \mu_{\star} \rangle_{\varpi} = \frac{1}{N} \sum_i^N \mu_{\star}(\varpi_i) \quad (\text{E.7})$$

$$\langle C_{\mu} \rangle_{\varpi} = \begin{pmatrix} \sigma_{\mu_{\text{RA}}|\varpi}^2 & \sigma_{\mu_{\text{RA}}, \mu_{\text{DEC}}|\varpi}^2 \\ * & \sigma_{\mu_{\text{DEC}}|\varpi}^2 \end{pmatrix} \quad (\text{E.8})$$

$$\sigma_{x, y|\varpi}^2 = \frac{N}{N-1} (\langle x_{\star} y_{\star} \rangle_{\varpi} - \langle x_{\star} \rangle_{\varpi} \langle y_{\star} \rangle_{\varpi}) \quad (\text{E.9})$$

These sample estimates were calculated from 10 parallax samples per star. We note that this estimation needs to be evaluated at each step of the optimization, making this the main computational bottleneck. The number of parallax samples was chosen to strike a balance between computational feasibility and statistical precision.

Appendix F: Noise estimation results

As discussed in Sect. 3.3.3, we have introduced a noise estimation factor η to the observational noise to correct for the possible systematic error introduced by binaries. In Fig. F.1, we relate the inferred η factors with the observed RVs and the respective observational noise. For most stars, the noise statistics do not change, i.e., they have an η value of the order of 1. Data points with very to extremely small uncertainties (from about 0.5 km s^{-1} to 0.001 km s^{-1}) are almost always down-weighted, indicating that the RV values are inconsistent with the surrounding RV field at the precision given by the noise. However, these data points are still informative, as the η factors only bring these error bars to the level of the bulk of the RV measurements in Sco-Cen. Most stars have an observational noise between 0.5 km s^{-1} to 10 km s^{-1} . In this regime, we see an increasing trend in that stars with high η values also have very high absolute RV values, which likely indicates that they are kinematic outliers. This gives good evidence that the automatic down-weighting using the noise estimation works. In the high noise regime, almost no stars are down-weighted with high η values. These stars likely have almost no impact on the analysis due to the already small likelihood value, making further outlier rejection unnecessary.

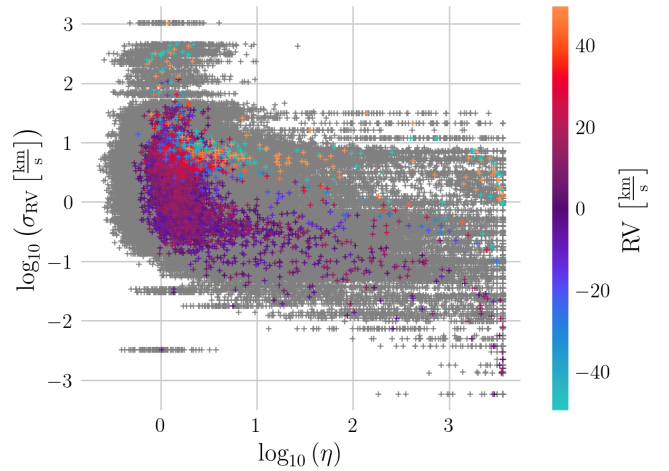


Fig. F.1: Noise estimation results. The plot shows the inferred noise estimation factors η per RV measurement versus the log-scaled observed uncertainties. The observed RV data are shown as a color scale. The scale is saturated at $\pm 50 \text{ km s}^{-1}$. The posterior samples of η are in gray, thereby illustrating the statistical uncertainties of the result.

Appendix G: Component fields

We show the component fields of the main vector field in Figs. A.4, A.5 and A.6. These plots give a supplementary viewpoint to the power spectrum plots in Fig. 4 and the full vector field plotted in Fig. 3a. The inside-out acceleration pattern of Sco-Cen is again nicely visible in all components.

Appendix H: Additional vorticity and divergence fields

Figure A.7 shows the vorticity of the main flow field of Sco-Cen. This plot reveals many small-scale structures. In general, it can be noted that many of the vorticity vectors seem to be parallel or anti-parallel to the direction connecting negative x , y , z , with the more positive values on the respective axes, which, at least for x and y , is the direction of Galactic rotation. A more detailed analysis of the vorticity will follow in Paper III. We furthermore show the divergence and vorticity maps of the secondary and δ fields in Fig. A.8.